June 2009

Rain/wind induced vibrations of stay-cables


(BaiChay Bridge, 2009)

by

Jesper Jensen

&

Claus Gadegaard

Master thesis

Aalborg University

Departement of Civil Engineering

International Master of Science Program

Department of Civil Engineering

Sohngaardsholmvej 57 9000 Aalborg, Denmark

www.imsc.aau.dk

Title:

Rain/wind induced vibrations of stay-cables

Project term:

B10K semester, spring 2009

Abstract:

Rain/wind induced vibrations for the most severe natural load on cables used as support will be examined. The theory behind rain/wind induced vibrations on stay-cables will be outlined, based on the present available literature. A numerical quasi-static multi degree of freedom model of a stay cable is developed and a load model is established to implement the rain/wind induced aeroelastic loading on the cable.

Four different types of damping mechanisms are considered for mitigation of the rain/wind induced vibrations. Active control of the axial forces by an actuator at the lower cable support point is initially considered. The control in the remaining three types is based on a perpendicular connection between the damping mechanism and the cable, at a constant distance away from the lower cable support point. Here, passive viscous damping is introduced where the damping coefficient is tuned to the first in-plane cable mode of vibration. Semi-active MR-damping is introduced with the objective to reduce the vibration response from passive viscous control. Finally, active control by use of the pole placement method is analysed. Furthermore, the active control by pole placement is supported by integral control in order to remove a static offset of the cable displacement from the applied mean wind.

Special attention is brought to evaluate the relative effectiveness of the considered damping mechanisms. Practical considerations, general theory, and control algorithms with regard to the mentioned control strategies will be handled.

Writers:

Jesper Jensen

Claus Gadegaard

Supervisor:

Søren R.K. Nielsen, Prof. Dr. Techn.

Concluded: 16.06.2009

Copies: 5

Sheets: 58

Preface

The present master thesis has been carried out in the period February 2009 to June 2009 at the Department of Civil Engineering, Aalborg University, Denmark.

The report is built in such a way where figures and tables are listed in sequential order. Equations are given a chapter reference followed by an equation number reference. The two references are separated by a full stop and the equation numbering is listed in sequential order which is restarted in each chapter.

References are made by sir name of the first author followed by the year of publication. Further details may be found on the reference list in the end of the report.

The project has had specific focus on creating a numerical model to analyse the rain/wind induced vibrations of a stay cable. The program files may be found on the digital project library and for the printed editions on the enclosed CD which may be found in the end of the report.

We would like to thank our supervisor Prof. Dr. Techn. Søren R.K. Nielsen. Throughout the semester, his persistent encouragement and guidance has been greatly appreciated.

Jesper Jensen

Claus Gadegaard

Table of contents

1 Introduction

Many structures today use cables as vital structural elements, such as cable-stayed bridges, guyed masts, etc. Due to very low inherent damping and relatively low stiffness, the cables are disposed to various environment induced vibrations either caused by wind, combined rain- and wind, or by motions of the support-structure. In the end, this can lead to cable- and connection failure or cracked corrosion protection which altogether reduce the life span of the cable system.

Especially the simultaneous occurrence of moderate rain and wind has been given significant attention in recent years, as it is not yet fully understood. As *Hikami* observed in 1986, this type of event can lead to extreme cable vibrations, (Hikami, 1986). These rain/wind induced vibrations occur at wind speeds significantly lower than the design wind speed and thus have a high probability of occurrence. The rain/wind induced vibrations of stay-cables at a stay-cable bridge will be examined further in this thesis.

Several methods have been proposed as mitigation measures for these vibrations. Cable cross ties have a significant effect as it reduces the free length of the cables. However, the bridge aesthetics is by some considered to be violated, (Yamaguchi, et al., 1995). The same applies for fluid-can dampers or changed surface geometry of the cable which may also be difficult to implement as a subsequent installation. Transversely attached linear viscous dampers can be efficient, but the connection point is restricted to a level where access due to maintenance is still possible.

The point of attachment of the damper is of great importance regarding the damping efficiency. The maximum amount of added damping is proportional to the distance, relative to the total cable length, between the point of contact and the cable anchorage, (Krenk, 2000),(Kovacs, 1982). Generally, a viscous damper may be tuned to optimal performance in a single vibration mode of the cable. However, field observations of rain/wind induced vibrations show that many modes are involved. Actually, the vibrations appear in some cases as travelling waves along the cable. Hence, the efficiency of linear viscous damping for the observed multi-mode performance may be questioned. According to the above, the implementation of another damping mechanism could be interesting.

Semi-active dampers such as magneto-rheological (MR) or electro-rheological (ER) dampers have the potential to change the damper characteristics, and hence adjust to multi-mode behaviour. *Johnson*, *Baker*, *Spencer*, and *Fujino* claimed that the performance level from semi-active control is near what can be obtained from a comparable active device, (Johnson, et al., 2007). Significant merits are the significantly reduced power source and a mechanism which will work as a passive damper in case of power failure.

Furthermore, an active control of the damping mechanism may be implemented. By doing so, the damping properties of the lower important modes may be prescribed on the condition that the required power is available in the damper mechanism. In the present case, the control algorithm for the active controller is defined by the pole placement method.

Finally, several studies have been made on active control of cable vibrations by axial support motion, (Wang, et al., 2007),(Fujino, et al., 1993). This active vibration control seems to be fairly efficient, but it has a drawback with respect to the required power source needed. The underlying control laws are evaluated to determine if this type of damping should be considered.

According to the above, the mitigation of rain/wind induced vibrations will be investigated where passive viscous damping, semi-active MR damping, and active control is used in order to evaluate the relative effectiveness of the different damping mechanisms.

2 Rain/wind induced vibrations

Due to the rain, a water film is formed on the surface of the cable. A downward flow on the cable surface will be present due to gravity. Under combined rain and wind, a retarding upward flow will be generated due to wind friction on the upper windward area of the cable. In case of higher mean wind speed U_0 corresponding to supercritical Reynolds numbers, the point of separation moves backward which may also lead to an upward flow due to wind friction on the lower leeward side of the cable. In a certain wind speed range, the stabilizing upward flow creates an equilibrium state where water stowage leads to the formation of a rivulet. The centre angle θ_0 and θ_0^* which describe the static equilibrium position of the upper- and lower rivulet, respectively, are therefore merely expected to depend on the mean wind speed. The above is illustrated in figure 1.

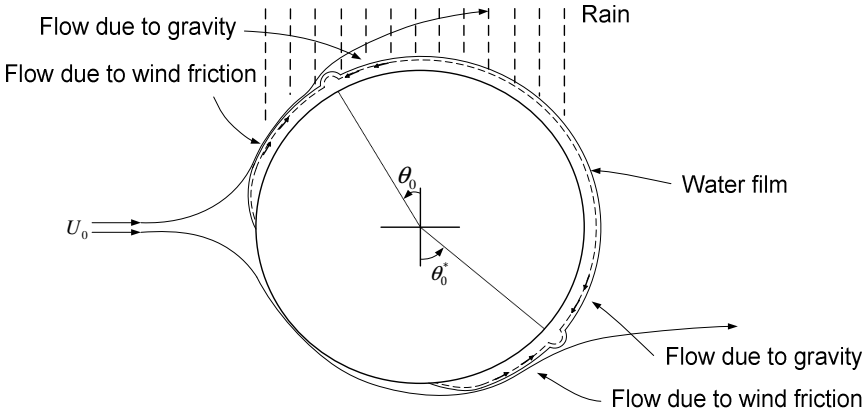

Figure 1: Formation of the upper rivulet due to water stowage.

It should be noted that rivulets may be formed at up to four different ranges of equilibrium positions, specified by the centre angle θ_0 and θ_0^*. These ranges are divided into two lower regions and two upper regions. The wind yaw angle β will naturally determine, in which regions of the cable the rivulets can be formed and only two rivulets may be present on a cable section at the same time, (Verwiebe, 1996), (Verwiebe, 1998). *Verwiebe's* test setup is illustrated in figure 2a where the cable is described in an (x, y, z)-coordinate system. The (x, y)-plane is placed in the static equilibrium plane of the cable. The x-axis is placed along the cable chord and has the inclination φ_0 with the horizontal plane. The y-axis is placed in the upwards direction and the z-axis is placed in the out-of-plane direction.

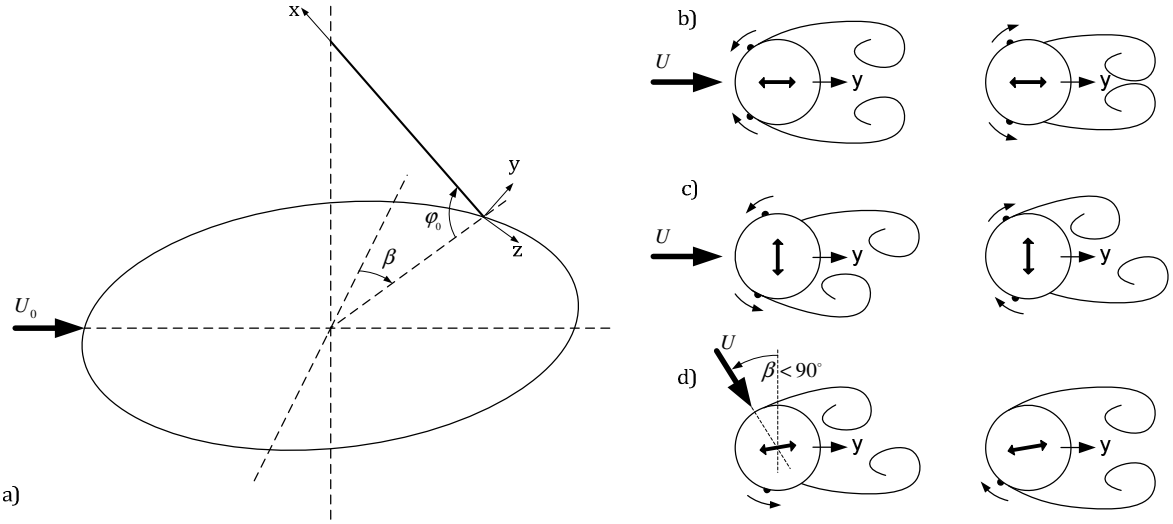

Figure 2: *Verwiebe's* model set up and some general findings.

The rivulets cause a modified surface that creates an unsymmetrical wind pressure distribution that can cause periodic exciting forces on the cable. This is understood in the way that uplift- and drag forces are changed according to a dynamic change in position of the rivulets. If these wind forces are changing resonance to the natural frequency of the cables, large vibrations can occur, (Verwiebe, 1996), (Verwiebe, 1998).

The results from *Verwiebe's* tests indicated that the phenomenon is characterized by in-plane- and out-of-plane vibrations governed by the wind yaw angle. The component U of the mean wind U_0 perpendicular to the cable, and the orbit of the cable vibrations are illustrated in figure 2b, figure 2c, and figure 2d. When $\beta = 90°$ and the rivulets oscillate symmetrically, in-plane vibrations occur as illustrated in figure 2b. When $\beta = 90°$ and the rivulets oscillate anti-symmetrically, out-of-plane vibrations occur as illustrated in figure 2c. When $\beta < 90°$ both in-plane- and out-of-plane vibrations exist, in which the in-plane vibrations are dominating, as illustrated in figure 2d.

It has been found both experimentally and numerically that maximum amplitudes occur when the cable angle of inclination $\varphi_0 = 30°$ and the wind yaw angle $\beta = \pm 35°$. Furthermore, results show that a rivulet along the upper part of the cable surface is the primary reason for rain/wind induced vibrations, (Hikami, 1986), (Gu, et al., 2004), (Gu, et al., 2008). *Hikami* and *Shiraishi* found a critical mean wind speed range of 9-15m/s, which is also considered in the following,(Hikami, et al., 1988). This is used in the following as to describe the most severe natural loading on a stay-cable.

2.1 Analytical models

In the past 20 years, different analytical models of the rain/wind induced vibrations have been devised. *Yamaguchi* developed one of the first models in 1990, illustrated in figure 3a, (Yamaguchi, 1990), where the asymmetric position of the rivulet causes galloping instability of the cable. The system is a SDOF system with a quasi-stationary laminar wind load applied. The model is strongly simplified as no structural damping is included, and the time varying displacement of the rivulet position not is considered.

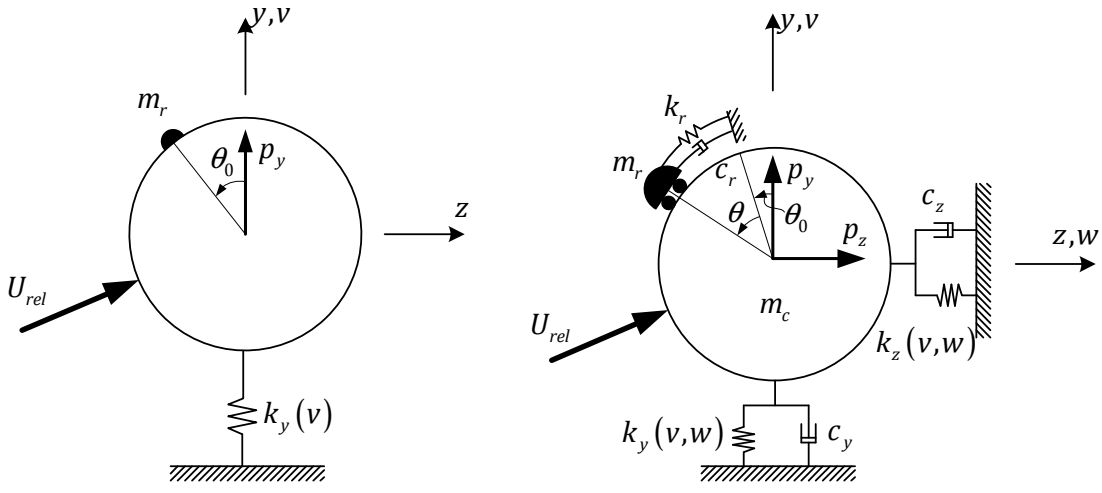

Figure 3: Analytical cable models.

The model by *Robra* showed in figure 3b is an extension of the *Yamaguchi* model, where an additional DOF for the motion of the rivulet is added, (Robra, 2003). The parameters m_c, k_y, k_z, c_y, c_z are to be interpreted as modal mass, stiffness and damping for the fundamental in-plane and out-of-plane motion, respectively. The motion of the rivulet is modelled by a nonlinear SDOF oscillator, driven by the motion of the cable. A further analysis of a 2DOF system is conducted in section 4.2. The vibration theory in *Robras* model is based on linear theory. However nonlinear geometric stiffness terms may easily be included.

Even more advanced models have been developed, where the wind force on the rivulet is included and some models have more than one rivulet. Because of the complicated models, the equation of motion is described by non-linear theory why wind tunnel tests are needed in order to determine the aerodynamic dependencies of the rivulet positions.

2.2 Numerical model

In the following analysis a numerical quasi-static MDOF model will be developed, describing a stay-cable at a stay-cable bridge under influence of rain/wind induced vibrations. The nonlinear geometric coupling between in-plane and out-of-plane vibrations will not be accounted for and only in-plane vibrations will be considered.

The cable mechanics is described in three different coordinate systems. (X, Y, Z) is a global Cartesian coordinate system which describes the equilibrium state. The (X, Y)-plane is placed in the static equilibrium plane of the cable. The X-axis is horizontal, and the Y-axis is orientated in the vertical direction. The origin is placed at the lower end of the cable. The (x, y, z)-coordinate system is a global auxiliary coordinate system with the same origin as the (X, Y, Z)-coordinate system. The (x, y)-plane is placed in the static equilibrium plane and the x-axis is placed along the cable chord, which has the inclination φ_0 to the X-axis. The (x', y', z')-coordinate system is a local coordinate system for each cable element with origin at the lowest end. The (x', y')-plane is placed in the static equilibrium plane of the cable and each local x'-axis is placed along the element chord, which has the inclination φ_e to the X-axis. Furthermore, L is the chord length, f is the sag of the cable, F_0 is the prestressing force, and g is the acceleration of gravity. The above is illustrated in figure 4.

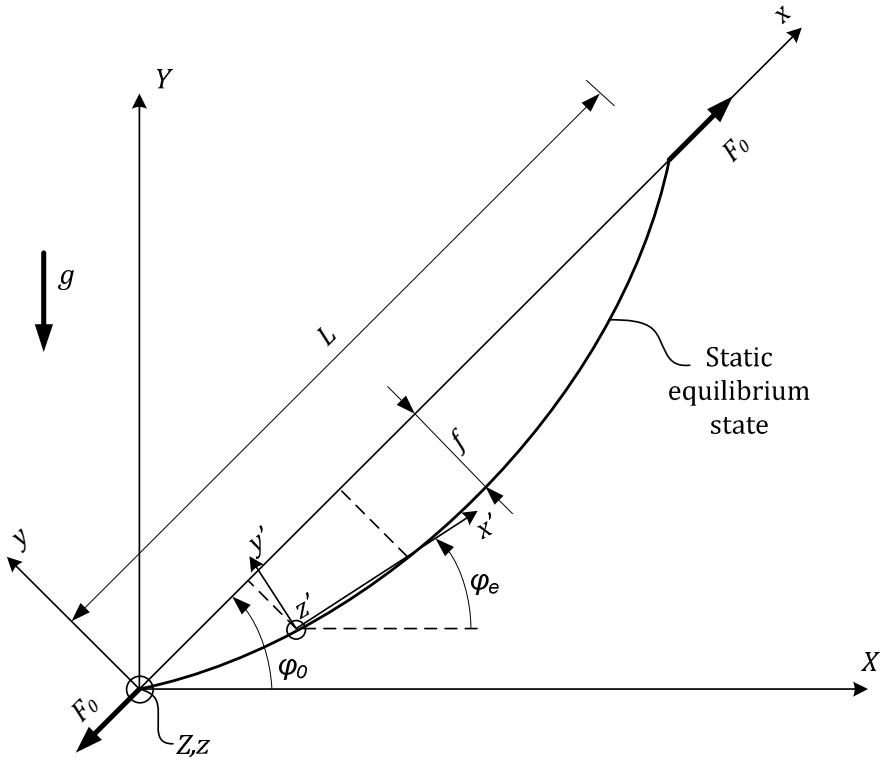

Figure 4: Global Cartesian-, global auxiliary-, and local coordinate system.

The mentioned MDOF model will be formulated by the finite element method, where the continuous cable system is subdivided into a finite number of elements. The rain/wind induced aeroelastic loading on the cable finite element is accounted for by also including the motion of the rivulet. The numerical model is described in chapter 4.

In what follows all capital bold letters denotes a matrix, lower case bold letters denotes a vector, and italic letters denotes a scalar.

3 Vibration control of shallow cables

As mentioned in chapter 1 the mitigation of cable vibrations will be investigated by passive viscous damping, semi-active MR-damping, and active control. The control strategies take into consideration the response of the system by use of sensors, i.e. both collocated and state feedback control is considered. The damping types are defined according to the amount of energy used when active and will be described in the following section.

A segment of a cable stayed bridge with the considered damper types installed is illustrated in figure 5. The control of axial forces works as illustrated in figure 5b while the remaining control types work as illustrated in figure 5a. Here $e(t)$ is a non-dimensional representation of the chord elongation, a is the distance between the connection of the damper and the lower support point of the cable, Ψ is the inclination angle of the damper with horizontal, v_d and $\dot{v}_d$ is the cable displacement and cable velocity in the direction of the damper, respectively, and $u(t)$ is the damper force.

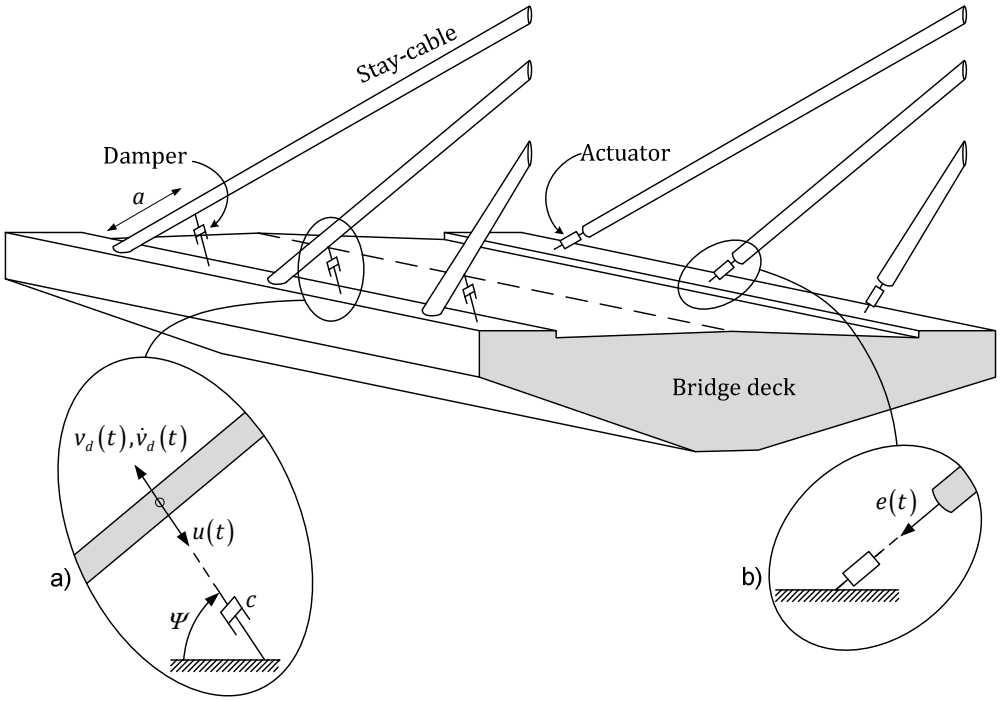

Figure 5: Damping mechanisms installed on a cable stayed bridge.

In figure 5a, only one damper is installed on each cable, but often two dampers are used to account for both in-plane and out-of-plane vibrations. These dampers will be placed in an inverted V-shape at the same connection point. In this report only in-plane vibrations are considered, why only one damper is included.

It should be noted that the control laws of the passive and semi-active dampers, as described in section 4.3.1 and 4.3.2, depend merely on local kinematics of the support point of the damper on the cable - as measured by the local damper elongation $v_d(t)$ and velocity $\dot{v}_d(t)$, i.e. the control is collocated. The active controls on the other hand, require that the total state of the cable is known at a given time for which the active controls are not collocated.

In what follows the uncontrolled system will be referred to as the open loop system while the controlled system will be referred to as the closed loop system. The damping mechanisms of each of the control strategies will be treated in the following.

3.1 Passive dampers

The passive dampers are characterised by suppressing vibrations without any supplied external energy. One of the simplest passive dampers (and the only one considered in this thesis) is the linear viscous damper, where a fluid, often oil, is compressed by a piston. Depending on the damper type, the fluid is

pressed trough some valves, which sizes and the viscosity of the fluid, determine the damping characteristics. The structure of the damper and the viscosity of the oil must be carefully chosen. It must neither be too rigid nor too compliant, but should be made as an optimum which lies in between. The characteristics of the damper are fixed and fitted to the characteristics of the cable, usually the fundamental mode of vibration.

3.2 Semi-active dampers

Semi-active dampers are characterized by having the capability of changing the properties for a system with relative large control effect in response of a command signal and very little energy input. The properties and the background for semi-active damping mechanisms are outlined in the following, based on, (Srinivasan, et al., 2001).

The MR-damper operates by use of a fluid which properties changes in response to an applied magnetic field. Similar to the MR-fluids, ER-fluids are applied an electric field instead. In the following only MR-fluids will be considered, but the physics of MR- and ER-fluids are almost identical.

The most remarkable property of the MR-fluids is the field-induced change of the ability to support a tremendous increase or decrease in shear stress. This ability is the result of the formation of particles within a fluid in response to the magnetic field. A typical MR-fluid consists of 20-40% iron particles of size 1 to 10μm added to a fluid, often mineral oil or silicon oil. Besides the iron particles, most MR-fluids also contain a small amount of additives that prevents the particles from setteling and to effect the polarization. These may however be neglected in most modelling.

An MR-fluid may in absence of the magnetic field be characterized as a Newtonian fluid, as resisting a shear strain γ with a shear stress τ proportional to the product of the strain rate $\dot{\gamma}$ and viscosity η

$$\tau = \eta \dot{\gamma} \tag{3.1}$$

This is acknowledged as an approximation, since most MR-fluids are in fact non-Newtonian because of the large amount of solid particles. The field-induced component of the shear stress is however often much larger than the $\eta\dot{\gamma}$ term, why (3.1) is an adequate model of the rate-dependent part of the total shear stress, also illustrated in figure 6.

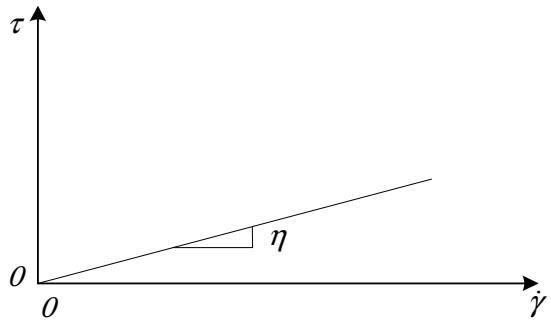

Figure 6: A Newtonian fluid shears at a rate proportional to stress.

The purpose of applying a magnetic field to the MR-fluid is to create chains in the direction of the magnetic field. The creation of the chains occurs in a few milliseconds and when there is no motion of the fluid or the walls surrounding the fluid, the chains are static structures that span the gap between the poles. The scenario is illustrated in figure 7, where a magnetic field is applied on a valve.

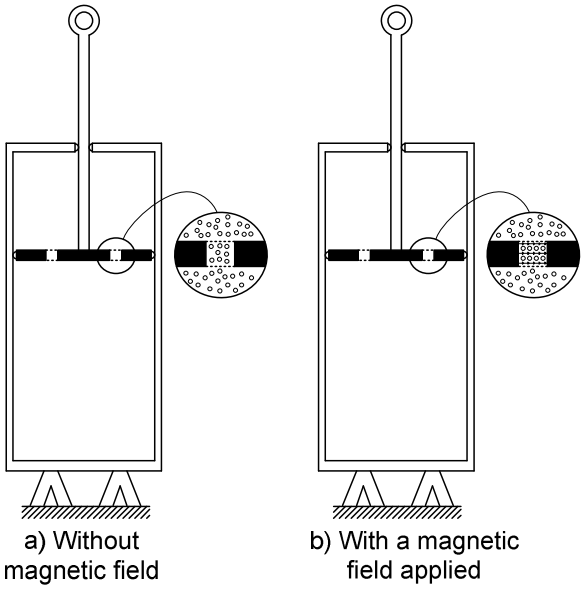

Figure 7: Effects when a magnetic field is applied to the MR-fluid.

Because of the created chains, shear strain occurs in the fluid that passes the valves and a shear stress distribution develops across the fluid. According to the strength of the field, the created chains will break and new chains will be created. The continual breaking and reforming of these particle chains results in a force resisting the motion of the fluid, and give rise to the field-dependent component of the shear stress τ. In most cases this component is much larger than the viscous shear stress $\eta\dot{\gamma}$. It is this large controllable shear stress that makes these fluids useable in mechanical systems.

It might be expected that the viscosity of the MR-fluid increases as a result of the formed chains, but this is not the case. The slope of the shear stress development, the viscosity η, changes very little if at all. The chains create instead a shear stress that is independently of the strain rate, this is also referred to as the yield stress τ_y. If the yield stress is added to the Newtonian model (3.1), the following Bingham stress-strain rate appear

$$\tau = \tau_y(H) + \eta\dot{\gamma} \tag{3.2}$$

where H represents the strength of the applied magnetic field. The response of the model is plotted in figure 8, which is the by far the most popular model used in modelling of MR-fluids.

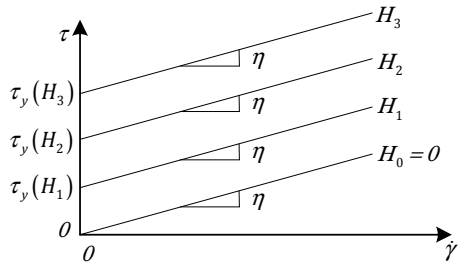

Figure 8: Shear stress versus shear strain rate for the Bingham model.

The design of the MR-damper is basically the same as for the linear viscous damper, where a piston forces a fluid through some valves. The advantage of the MR-damper is that the damping coefficient is changeable, by changing the magnetic field surrounding the MR-fluid. Additionally, a hystereric friction damping component may be introduced.

The amount of energy needed to control the magnetic field is very small, and often small batteries have sufficient amount of power. If, by some reason, the power supply to the mechanism is cut off, the MR-damper should be tuned in the same way as an optimal viscous damper. Hereby, the stand-by position has the same abilities as a linear viscous damper.

3.3 Active control

In active control a controller-chosen number of modes of vibration are controlled actively by applying a control force. The active control mechanism is in contrast to the passive and the semi-active damper characterized by use of a relative large amount of energy. Therefore, it is often necessary to connect the actuators to an external power supply. Two active control mechanisms are considered in this thesis. One is control of axial forces and the other operates by use of an actuator installed similar as the above mentioned dampers.

The control of axial forces operates by control of the elongation of the cable ΔL through an actuator at one of the support points. Hereby, a variation in the tension F_0 is generated through the cable. By applying a control law for these elongations, the vibrations of the cable may be damped.

By increasing the modal damping ratio of selected modes an asymptotical stability of the system can be reached. One approach of doing so is by use of the pole placement method, as introduced in section 4.3.3.

As opposed to the semi-active MR-damper, the active controllers have no direct safety mechanism in case of power failure. Instead of having the same abilities as a viscous damper when no power is applied, the actuator will either lock the cable or have no resistance at all, which is a drawback.

4 Numerical modelling

To formulate the equation of motion for the stay-cable it is necessary to determine the load caused by the oscillating rivulet. The cable is assumed only to be inflicted by a constant static mean wind load, which entail that the only change in the load on the cable is based on the change in the position of the rivulet.

4.1 Modelling of the rain/wind induced loading

The load model for the rain/wind induced aeroelastic loading will be presented, presuming that merely a single rivulet is influencing the flow pattern around the cable.

The rain/wind induced force on the cable is a contribution of a lift- and drag force which depends on the wind angle of attack and the flow conditions. Static wind tunnel tests are used to determine the lift- and drag coefficient dependencies which will be described initially.

4.1.1 Description of static wind tunnel tests

The following rely on the tests performed by *Gu, Du, and Li*, (Gu, et al., 2008). In the tests the rivulet is represented by a semi-circle with the radius r and the position given by the centre angle α, while the cable cross sectional radius is denoted R. The undisturbed wind flow have mean wind speed U_0. The geometrical parameters and the assumed development of the streamlines in the upper side of the boundary layers are illustrated in figure 9. As seen, the rivulet on the upper half of the cross section is expected to create an earlier point of separation than for the lower part.

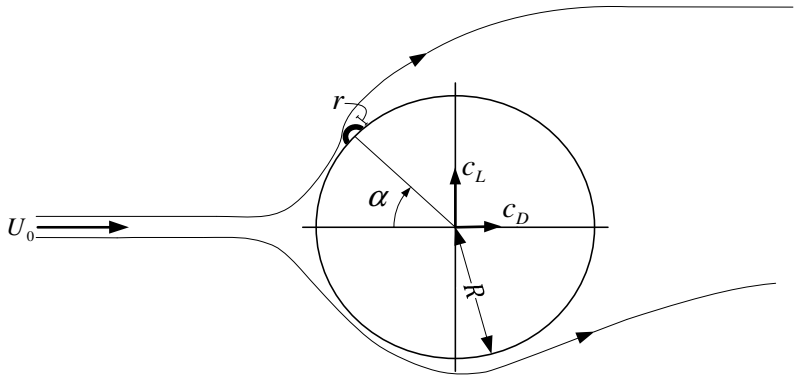

Figure 9: 2D representation of the wind tunnel tests.

As mentioned in chapter 2 the rain/wind induced vibration problem is caused by the formation and oscillation of the rivulet. Based on dimensional analysis the time dependent lift- and drag coefficients may be given as

$$\begin{aligned} c_D &= c_D\left(\alpha, Re, St, t, \frac{r}{R}\right) \\ c_L &= c_L\left(\alpha, Re, St, t, \frac{r}{R}\right) \end{aligned} \tag{4.1}$$

where Re is Reynolds number, St is the Strouhal number, and t is the time. Re is defined as

$$Re = \frac{U_0 2R}{\upsilon} \tag{4.2}$$

where υ is the kinematic viscosity of air. As mentioned in chapter 2, the considered domain of the critical mean wind velocity is $9 - 15\,m/s$ and in this report the radius of the cable cross section R is considered around $5 - 9cm$. The considered temperatures are in the range of $5°C - 20°C$ which leads to kinematic viscosities in the range $1.3 \cdot 10^{-5}\,m^3/s \leq \upsilon \leq 1.5 \cdot 10^{-5}\,m^3/s$. Then, the maximum value of Re becomes $Re \approx 1.6 \cdot 10^5$. The transition from laminar to turbulent boundary layer flow is near $Re = 5 \cdot 10^5$ which

implies a flow in the subcritical domain with laminar attached boundary layer. Then, the dependence of Re is small, and hence it is ignored as an independent variable of the aerodynamic coefficients, (Peil, et al., 2007). Further, St is constant and approximately equal to 0.20 throughout the sub-critical domain.

The relative rivulet magnitudes are in the range $r/R \in [0.01\,,0.10]$. Model tests show that c_L and c_D depend very little on the actual magnitude of the rivulet in this interval, (Gu, et al., 2008). This suggests that the effect of the rivulet merely is to cause a separation of the upper boundary layer as illustrated in figure 9.

The explicit dependence of t is partly due to rhythmic vortex shedding, and partly due to turbulence in the incoming wind field. The vortex shedding is assumed to be periodic with the Strouhals angular frequency ω_S given as

$$\omega_S = 2\pi St \frac{U_0}{2R} \simeq 0.63 \frac{U_0}{R} \tag{4.3}$$

The above observations leads to the following reduced expression of (4.1)

$$\begin{aligned} c_L(\alpha,t) &= c_L(\alpha,t+T_S) \\ c_D(\alpha,t) &= c_D(\alpha,t+T_S) \end{aligned} \tag{4.4}$$

where $T_S = 2\pi/\omega_S$. As the vortex shedding is assumed to be periodic, a Fourier series may be used to decompose the expressions in (4.3) and (4.4). It is well known that $c_L(\alpha,t)$ is dominated by the 1st harmonic and $c_D(\alpha,t)$ by the 2nd harmonic in the Fourier series expansion, (Prostas, et al., 2003). This suggests the following approximate expressions

$$\begin{aligned} c_L(\alpha,t) &\simeq c_{L,m}(\alpha) + c_{L,1}(\alpha)\cos\left(\omega_S t + \psi_L(\alpha)\right) \\ c_D(\alpha,t) &\simeq c_{D,m}(\alpha) + c_{D,2}(\alpha)\cos\left(2\omega_S t + \psi_D(\alpha)\right) \end{aligned} \tag{4.5}$$

where $c_{L,m}(\alpha)$ and $c_{D,m}(\alpha)$ represent the time-averaged mean values, $c_{L,1}(\alpha)$ and $c_{D,2}(\alpha)$ are the dominating harminic amplitudes, and $\psi_L(\alpha)$ and $\psi_D(\alpha)$ are the related phases. The most correct way would be to apply the models (4.5) in the dynamic analysis. As no data of the Fourier amplitudes and phases are available in the achieved literature this approach has not been possible. In the achieved literature, merely the RMS-values $\bar{c}_L$ and $\bar{c}_D$ are indicated. These are related to (4.5) as follows

$$\begin{aligned} \bar{c}_L(\alpha) &= \sqrt{\frac{1}{T_S}\int_0^{T_S} c_L^2(\alpha,t)\,dt} = \sqrt{c_{L,m}^2(\alpha) + \frac{1}{2}c_{L,1}^2(\alpha)} \\ \bar{c}_D(\alpha) &= \sqrt{\frac{1}{T_S}\int_0^{T_S} c_D^2(\alpha,t)\,dt} = \sqrt{c_{D,m}^2(\alpha) + \frac{1}{2}c_{D,2}^2(\alpha)} \end{aligned} \tag{4.6}$$

The test results are obtained by pressure taps mounted on the cable periphery as illustrated in figure 10. Here, $p_i(t)$ is the pressure and $\theta_{P,i}$ is the centre angle of the i^{th} pressure tap, and p_0 is the referential pressure. The pressure coefficient $c_{p,i}$ in the i^{th} pressure tap is determined as follows

$$c_{p,i}(t) = \frac{p_i(t) - p_0}{\frac{1}{2}\rho U_0^2} \tag{4.7}$$

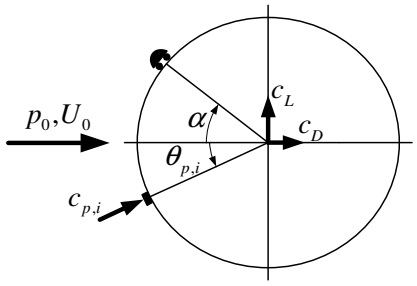

Figure 10: Definition of pressure at the i^{th} pressure tap.

The pressure coefficients are used to determine c_L and c_D by integration on the cable circumference as

$$c_L(\alpha,t) = \int_0^{2\pi} c_P(\theta_P,t)\sin\theta_P d\theta_P$$
$$c_D(\alpha,t) = \int_0^{2\pi} c_P(\theta_P,t)\cos\theta_P d\theta_P \quad (4.8)$$

This procedure must be repeated while varying the position of the artificial rivulet, as given by the angle α. The variation of the aerodynamic coefficients as function of rivulet position is hereby clarified.

4.1.2 Interpretation of test results

Figure 11 shows the variation of the RMS values $\bar{c}_L$ and $\bar{c}_D$ as a function of the angle of attack α.

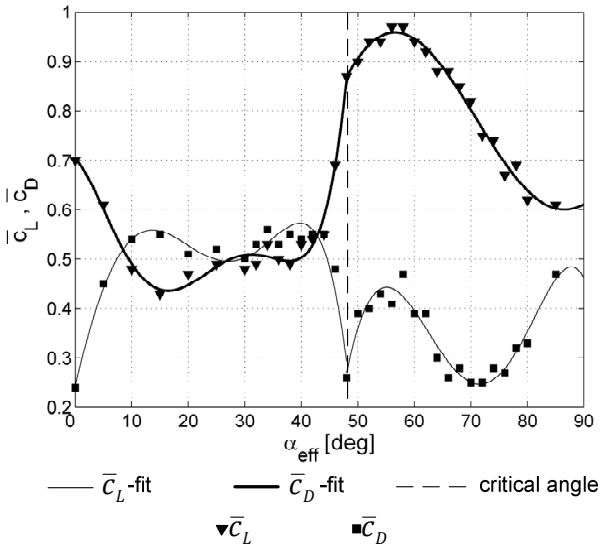

Figure 11: Variation of the lift- and drag coefficients.

The significant drop in c_L and increase in c_D, in the vicinity of the critical angle of attack α_{cri}, are observed in all the tests within the range $10° \leq \alpha \leq 48°$ and cannot be consideret as an outlier which was initially expected. In order to illustrate the observed rapid variation of c_L and c_D, the pressure distribution on the cable surface is presented in figure 12. The three distributions are representative for the position of the rivulet in the following segments which is illustrated by hatched areas in figure 12:

- figure 12a: $0° \leq \alpha < 10°$
- figure 12b: $10° \leq \alpha < 48°$
- figure 12c: $48° \leq \alpha \leq 90°$

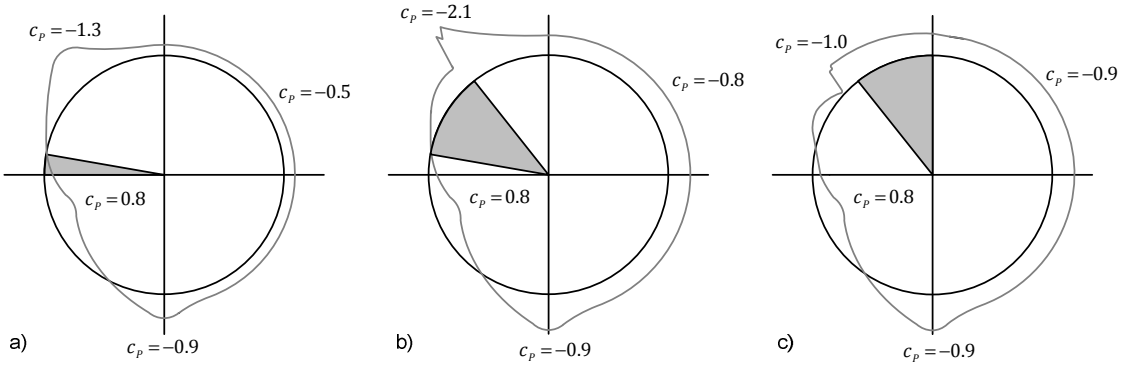

Figure 12: Pressure distributions on the cable surface as a function of the rivulet position.

The governing expressions for $\bar{c}_L$ and $\bar{c}_D$ are fitted the points as illustrated in figure 11 by polynomials c.f. (4.9). The slope of the curves changes dramatically when $\alpha = \alpha_{cri} = 48°$. The expressions are therefore divided into two ranges distinguished by α_{cri}.

$$\begin{aligned} 0rad \le \alpha < 0.84rad \quad & \begin{cases} \bar{c}_L = 0.24 + 4.62\cdot10^{-2}\alpha - 9.55\cdot10^{-4}\alpha^2 - 1.1\cdot10^{-4}\alpha^3 + 5.1\cdot10^{-6}\alpha^4 - 5.83\cdot10^{-8}\alpha^5 \\ \bar{c}_D = 0.51 + 4.38\cdot10^{-2}\alpha - 0.15\alpha^2 - 3.21\cdot10^{-2}\alpha^3 + 0.16\alpha^4 + 6.21\cdot10^{-2}\alpha^5 \end{cases} \\ 0.84rad \le \alpha \le \frac{\pi}{2}rad \quad & \begin{cases} \bar{c}_L = 0.28 - 0.15\alpha + 0.16\alpha^2 + 9.1\cdot10^{-2}\alpha^3 - 5.52\cdot10^{-2}\alpha^4 \\ \bar{c}_D = 0.86 - 0.19\alpha - 5.79\cdot10^{-2}\alpha^2 + 4.63\cdot10^{-2}\alpha^3 + 5.78\cdot10^{-4}\alpha^4 \end{cases} \end{aligned} \tag{4.9}$$

4.1.3 Derivation of load model

In the following, the expressions (4.9) for the fitted $\bar{c}_L$ and $\bar{c}_D$ will be used to express the aerodynamic load on the cable in the local y'-direction of the cable finite element.

The following delimitations and assumptions are used in the load model.

- Quasi-static flow conditions for the RMS values of the lift- and drag coefficients
- The upper rivulet is assumed to be uniformly distributed along the longitudinal axis for each cable finite element and oscillates circumferentially over the cable surface
- Turbulent effects and axial flow effects are not considered
- The cable chord inclination φ_e is considered to be constant for the considered cable finite element
- The elasticity of the cable supports due to the flexibility of pylons and bridge deck are not included
- The mean wind speed U_0 is assumed constant along the discretized cable even though the wind profile change with height

The quasi-static approximation entail that memory effects on the aerodynamic coefficients are ignored. This implies that the change in $\bar{c}_L$ and $\bar{c}_D$ over time, when the angle of attack varies, is assumed to take place momentarily. This simplification will be commented in section 4.1.4.

In what follows, U_{rel} is the mean wind speed relative to the moving cable, α_0 is the angle of attack between U and the static position of the rivulet θ_0, θ is the dynamic increment of the rivulet centre angle, γ is the angle between U and the z'-axis, and α_{eff} signifies the effective, static angle of attack between U_{rel} and the displaced position of the rivulet. The above is illustrated in figure 13 which is used to clarify the relation between cable- and rivulet motions in the following.

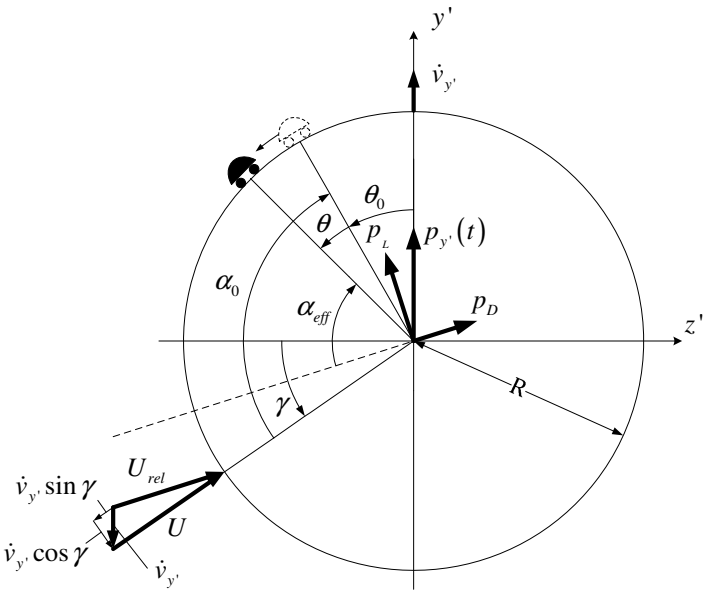

Figure 13: Definition of parameters used in the load model.

As illustrated, the drag- and lift forces per unit of length, p_L and p_D are perpendicular and parallel to the relative wind velocity U_{rel}, respectively. An expression for U_{rel} is therefore sought initially. U is related to the undisturbed mean wind velocity U_0 as follows

$$U = U_0\sqrt{\cos^2\beta + \sin^2\varphi_0\sin^2\beta} \tag{4.10}$$

The angle γ is expressed as

$$\gamma = \sin^{-1}\left(\frac{\sin\varphi_0\sin\beta}{\sqrt{\cos^2\beta + \sin^2\varphi_0\sin^2\beta}}\right) \tag{4.11}$$

Assuming $|\dot{v}_{y'}| \ll U$, the relative wind velocity may be linearized as follows, c.f. figure 13.

$$\begin{aligned} U_{rel}^2 &= \left(U - \dot{v}_{y'}\sin\gamma\right)^2 + \left(\dot{v}_{y'}\cos\gamma\right)^2 \\ &\simeq U^2\left(1 - 2\sin\gamma\frac{\dot{v}_{y'}}{U}\right) \end{aligned} \tag{4.12}$$

where $\dot{v}_{y'}$ is the velocity of the cable finite element in the local y'-direction. The effective angle of attack between the relative wind velocity and the position of the displaced rivulet becomes

$$\alpha_{eff} = \alpha_0 + \Delta\alpha \tag{4.13}$$

where

$$\begin{aligned} \alpha_0 &= \frac{\pi}{2} + \gamma - \theta_0 \\ \Delta\alpha &= -\cos\gamma\frac{\dot{v}_{y'}}{U} - \theta \end{aligned} \tag{4.14}$$

The centre angles defining the static position of the rivulet θ_0 and the dynamic oscillation of the rivulet θ are considered positive counter clockwise. The lift- and drag coefficients are supposed to depend merely on the present value of α_{eff} due to a quasi-static assumption. If the dynamic increment fulfils $|\Delta\alpha| \ll 1$, $\bar{c}_L$ and $\bar{c}_D$ may be linearized around the static angle of attack α_{eff}. In combination to the linearization of U_{rel}^2

as given in (4.12) this provides the following linearized expressions for the lift- and drag force per unit of length.

$$\begin{aligned} p_L &= \rho U_{rel}^2 R \bar{c}_L\left(\alpha_{eff}\right) \\ &\simeq \rho U^2 R\left(1-2\sin\gamma\frac{\dot{v}_{y'}}{U}\right)\left(\bar{c}_{L,0}-\frac{\partial \bar{c}_{L,0}}{\partial\alpha}\left(\cos\gamma\frac{\dot{v}_{y'}}{U}+\theta\right)\right) \\ &\simeq \rho U^2 R\left(\bar{c}_{L,0}-\left(2\sin\gamma\bar{c}_{L,0}+\cos\gamma\frac{\partial \bar{c}_{L,0}}{\partial\alpha}\right)\frac{\dot{v}_{y'}}{U}-\frac{\partial \bar{c}_{L,0}}{\partial\alpha}\theta\right) \end{aligned} \tag{4.15}$$

$$\begin{aligned} p_D &= \rho U_{rel}^2 R \bar{c}_D\left(\alpha_{eff}\right) \\ &\simeq \rho U^2 R\left(\bar{c}_{D,0}-\left(2\sin\gamma\bar{c}_{D,0}+\cos\gamma\frac{\partial \bar{c}_{D,0}}{\partial\alpha}\right)\frac{\dot{v}_{y'}}{U}-\frac{\partial \bar{c}_{D,0}}{\partial\alpha}\theta\right) \end{aligned} \tag{4.16}$$

where $\bar{c}_{L,0}=\bar{c}_L(\alpha_0)$ and $\bar{c}_{D,0}=\bar{c}_D(\alpha_0)$. The load per unit length $p_{y'}$ in the local y'-direction is obtained by projection of p_L and p_D in the y'-direction. Again a linearization is used to expand the sine and cosine functions around γ.

$$\begin{aligned} p_{y'} &= p_L\sin\left(\gamma-\cos\gamma\frac{\dot{v}_{y'}}{U}\right)+p_D\cos\left(\gamma-\cos\gamma\frac{\dot{v}_{y'}}{U}\right) \\ &\simeq p_L\left(\sin\gamma-\cos^2\gamma\frac{\dot{v}_{y'}}{U}\right)+p_D\left(\cos\gamma+\sin\gamma\cos\gamma\frac{\dot{v}_{y'}}{U}\right) \\ &\simeq p_{y',0}+p_{y',1}\dot{v}_{y'}+p_{y',2}\theta \end{aligned} \tag{4.17}$$

where

$$\begin{aligned} p_{y',0} &= \rho U^2 R\left(\bar{c}_{L,0}\sin\gamma+\bar{c}_{D,0}\cos\gamma\right) \\ p_{y',1} &= \rho U R\left(\left(1+\sin^2\gamma\right)\bar{c}_{L,0}+\frac{1}{2}\bar{c}_{D,0}\sin 2\gamma+\frac{1}{2}\sin 2\gamma\frac{\partial \bar{c}_{L,0}}{\partial\alpha}+\cos^2\gamma\frac{\partial \bar{c}_{D,0}}{\partial\alpha}\right) \\ p_{y',2} &= -\rho U^2 R\left(\sin\gamma\frac{\partial \bar{c}_{L,0}}{\partial\alpha}+\cos\gamma\frac{\partial \bar{c}_{D,0}}{\partial\alpha}\right) \end{aligned} \tag{4.18}$$

From (4.18), a static offset of the cable displacement is expected due to the static load term $p_{y',0}$. Based on a stability analysis of the boundary layer equations for the water film, it was shown by *Verwiebe* that up to four ranges of equilibrium positions defined by different centre angles θ_0 exist, (Peil, et al., 2007). The equilibrium positions are expected to depend merely on the mean wind speed, as investigated e.g. by *Hikami,* (Hikami, et al., 1988). The governing equation for $\theta_0=\theta_0(U_0)$ is fitted the results indicated in figure 14 by a 4th order polynomial.

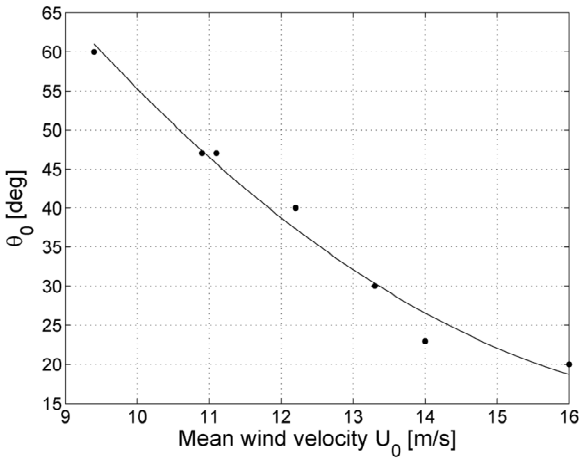

Figure 14: Static position of the upper rivulet as a function of the mean wind velocity, (Hikami, et al., 1988).

The test performed by *Hikami* and *Shiraishi* was performed for one specific set-up only. However, this is the only achieved information for which it is used in the following.

4.1.4 Memory effect and non-stationarity

As mentioned, the considered load model assumes quasi-stationary conditions. The aerodynamic forces are hereby assumed to change momentarily due to changes of the effective angle of attack. In reality the non-stationary flow around the cable will not adjust to the new flow conditions until the elapse of some time. This transient phase is displayed as a memory effect on the lift- and drag coefficients.

A suitable upgrade to the numerical model would be to take this memory effects into consideration. Experimental results would be necessary for this to be implemented, which are not available. However, a brief exposition of the issue is made for the lift-coefficient, and the principle is assumed to be similar for the drag-coefficient. An increment $d\alpha_{eff}(\tau)$ of the effective angle takes place at some time $\tau < t$ prior to the present time t. Due to the transient establishment of stationary flow conditions, the corresponding increment of the lift coefficient $dc_L(t)$ is delayed as given as

$$dc_L(t) = \frac{dc_L(\alpha_0)}{d\alpha}\Phi_L(t-\tau)d\alpha_{eff}(\tau) \tag{4.19}$$

where Φ_L represents a non-dimensional impulse response function, also named an indicial function, for the lift coefficient $c_L(t)$. The total non-stationary lift-coefficient at time t is obtained by superposition as

$$c_L(t) = c_L(\alpha_0) + \frac{dc_L(\alpha_0)}{d\alpha}\int_0^t \Phi_L(t-\tau)\dot{\alpha}_{eff}(\tau)d\tau \tag{4.20}$$

No exact information about the indicial function for this specific problem is available, for which reason the following is based on experience with aerofoils and general reasoning.

The Laplace transformation of the indicial function is approximated by means of a proper rational approximation

$$\Phi_L(s) = \frac{P(s)}{Q(s)} = \frac{p_0 s^m + p_1 s^{m-1} + \cdots + p_{m-1}s + p_m}{s^n + q_1 s^{n-1} + \cdots + q_{n-1}s + q_n} \tag{4.21}$$

The coefficients p_0,..., p_m and q_0,..., q_n are real and $m \leq n$. The indicial function is not assumed to represent an oscillatory response for which reason all poles are assumed to be non-positive real valued.

$$\begin{aligned}\mathrm{Re}\left(s_j\right)&\le 0\\ \mathrm{Im}\left(s_j\right)&=0\end{aligned} \tag{4.22}$$

Further, the limit $\Phi(t\to\infty)=1$ implies that a zero pole $s=0$ must exist corresponding to $q_n=0$. Then, (4.21) is equivalent to the following expansion in partial fractions

$$\Phi_L(s)=\frac{1}{s}-\sum_{j=2}^{n}\frac{a_j}{s_j}\frac{1}{s-s_j} \tag{4.23}$$

where a_j are real constants. The inverse Laplace transformation provides the following expression for $\Phi_L(t)$

$$\Phi_L(t)=1-\sum_{j=2}^{n}\frac{a_j}{s_j}e^{s_j t} \tag{4.24}$$

Next, (4.24) is inserted into (4.20)

$$\begin{aligned}c_L(t)&=c_L(\alpha_0)+\frac{dc_L(\alpha_0)}{d\alpha}\left(\alpha_{eff}(t)-\sum_{j=2}^{n}\frac{a_j}{s_j}\int_0^t e^{s_j(t-\tau)}\dot{\alpha}_{eff}(\tau)d\tau\right)\\ &=c_L(\alpha_0)+\frac{dc_L(\alpha_0)}{d\alpha}\left(\alpha_{eff}(t)-\sum_{j=2}^{n}\frac{a_j}{s_j}\left(e^{s_j(t-\tau)}\alpha_{eff}(\tau)\Big|_0^t-\int_0^t\left(-s_j\right)e^{s_j(t-\tau)}\alpha_{eff}(\tau)d\tau\right)\right)\\ &=c_L(\alpha_0)+\frac{dc_L(\alpha_0)}{d\alpha}\left(\alpha_{eff}(t)\left(1-\sum_{j=2}^{n}\frac{a_j}{s_j}\right)-\sum_{j=2}^{n}\frac{a_j}{s_j}e^{s_j t}\alpha_{eff}(0)-\sum_{j=2}^{n}a_j\int_0^t e^{s_j(t-\tau)}\alpha_{eff}(\tau)d\tau\right)\\ &=c_L(\alpha_0)+\frac{dc_L(\alpha_0)}{d\alpha}\left(\alpha_{eff}(t)\Phi_L(0)-\left(1-\Phi_L(t)\right)\alpha_{eff}(0)-\sum_{j=2}^{n}a_j z_j(t)\right)\end{aligned} \tag{4.25}$$

The final expression for the lift-coefficient is only depending on α_{eff} and the state variables $z_j(t)$ defined by

$$z_j(t)=\int_0^t e^{s_j(t-\tau)}\alpha_{eff}(\tau)d\tau \tag{4.26}$$

Since no complex poles occur, the Φ_L function can be illustrated as in figure 15 where a dimensionless time variable has been introduced.

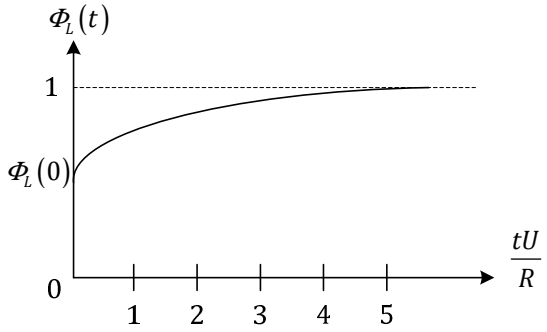

Figure 15: Qualitative dependence of $\Phi_L(t)$ as a function of time.

To implement the memory effect in the model, tests are to be made to determine the coefficients a_j and the poles s_j.

4.2 Structural modelling

A cable as described in section 2.2 is considered. The chord length is divided into n equivalent intervals $\Delta x = L/n$ which corresponds to $n+1$ equidistance nodes with $x_0 = 0$ and $x_{n+1} = L$. The end-points x_i and x_{i+1} of the i[th] interval defines the nodal points of the i[th] cable element as shown on figure 16. It should be noted that when the damper is accounted for, a correction could prove to be beneficial. Adding a separate damper node allows for a decrease in n, reducing the total computational time.

Each node has three degrees of freedom. Since the cable is fixed at the supports this implies that the cable has $m = 3(n-1)$ number of degrees of freedom. The sag of the cable is considered small compared to the chord length. As a consequence, the prestressing force along the chord in the static equilibrium state is assumed constant for all elements. Furthermore, a parabolic static suspension may be assumed, given by

$$y(x) = -4f\left(1 - \frac{x}{L}\right)\frac{x}{L} \tag{4.27}$$

The sag f is given as

$$f = \frac{1}{8}\frac{\mu g L^2}{F_0}\cos\varphi_0 \tag{4.28}$$

The length l_e of the cable element i and the inclination of the element φ_e in the static equilibrium state is defined as the angle from the local x'-axis to global x-axis positive in the z-direction. The following formulations are based on (Nielsen, 2004).

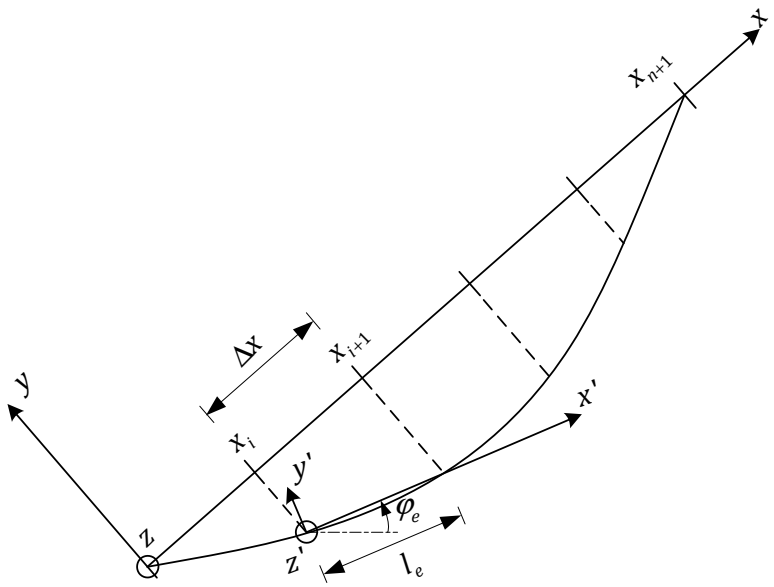

Figure 16: Cable shown in the global auxiliary coordinate system, discretisized in n elements.

A deformed cable element is illustrated in figure 17. The dynamic displacement vector of a particle with the referential position at x' is denoted $\mathbf{v}'_e(x',t)$ with local components $v_{x'}(x',t)$, $v_{y'}(x',t)$, and $v_{z'}(x',t)$. The external dynamic load vector per unit length of the referential static equilibrium suspension $\mathbf{p}'_e(x',t)$ has the local components $p_{x'}(x',t)$, $p_{y'}(x',t)$, and $p_{z'}(x',t)$. The element degrees of freedom are assembled in the vector $\mathbf{q}'^{T}_e(t) = [q'_1(t), \dots, q'_6(t)]$, where $q'_1(t), \dots, q'_6(t)$ signify the components of the end section displacements relative to the local (x', y', z') -coordinate system. The nodal reaction force vector conjugated to $\mathbf{q}'_e(t)$ is denoted $\mathbf{r}'_e(t)$ and contains the components $r'_1(t), \dots, r'_6(t)$.

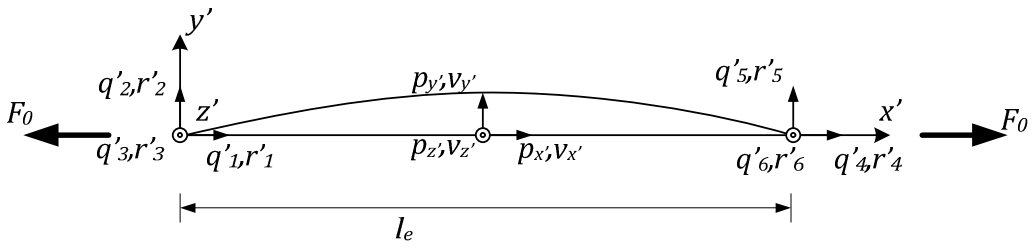

Figure 17: Cable element in the local coordinate system.

The displacement field $\mathbf{v}'_e(x',t)$ in local coordinates along the element is approximated by linear interpolation between the displacements of the end sections as

$$\mathbf{v}'_e(x',t) = \mathbf{N}(x')\mathbf{q}'_e(t) \tag{4.29}$$

The shape functions in the shapematrix $\mathbf{N}(x')$ are given as

$$\mathbf{N}(x') = \begin{bmatrix} N_1(x') & 0 & 0 & N_2(x') & 0 & 0 \\ 0 & N_1(x') & 0 & 0 & N_2(x') & 0 \\ 0 & 0 & N_1(x') & 0 & 0 & N_2(x') \end{bmatrix} \tag{4.30}$$

$$N_1(x') = 1 - \frac{x'}{l_e} \quad , \quad N_2(x') = \frac{x'}{l_e} \tag{4.31}$$

The local equation of motion for the element is formulated by Lagranges equation for the chosen degrees of freedom. The Lagrangian becomes

$$L_e(\mathbf{q}'_e, \dot{\mathbf{q}}'_e) = T_e(\dot{\mathbf{q}}'_e) - U_e(\mathbf{q}'_e) \tag{4.32}$$

where the kinetic energy $T_e(\dot{\mathbf{q}}'_e)$ and the potential energy $U_e(\mathbf{q}'_e)$, including the potential energy of the conservative external loads and reaction forces, are given as

$$\begin{aligned} T_e(\dot{\mathbf{q}}'_e) &= \int_0^{l_e} \frac{1}{2}\mu \left(\left(\frac{\partial v'_{x'}}{\partial t}\right)^2 + \left(\frac{\partial v'_{y'}}{\partial t}\right)^2 + \left(\frac{\partial v'_{z'}}{\partial t}\right)^2 \right) dx' \\ &= \frac{1}{2}\dot{\mathbf{q}}'^T_e(t)\mathbf{M}'_e\dot{\mathbf{q}}'_e(t) \end{aligned} \tag{4.33}$$

$$\begin{aligned} U_e(\mathbf{q}'_e) &= \int_0^{l_e} \frac{1}{2}\left(AE\left(\frac{\partial v'_{x'}}{\partial x'}\right)^2 + F_0\left(\frac{\partial v'_{y'}}{\partial x'}\right)^2 + F_0\left(\frac{\partial v'_{z'}}{\partial x'}\right)^2 \right) dx' - \int_0^{l_e} \left(p_{x'}v_{x'} + p_{y'}v_{y'} + p_{z'}v_{z'} \right) dx' \\ &= \frac{1}{2}\mathbf{q}'^T_e(t)\mathbf{K}'_e\mathbf{q}'_e(t) - \mathbf{q}'^T_e(t)\mathbf{p}'_e(t) - \mathbf{q}'^T_e(t)\mathbf{r}'_e(t) \end{aligned} \tag{4.34}$$

The consistent mass matrix $\mathbf{M}'_e$, stiffness matrix $\mathbf{K}'_e$ and nodal load vector $\mathbf{p}'_e$ of the structural element are given as follows

$$\mathbf{M}'_e = \int_0^{l_e} \mu \mathbf{N}_e^T(x') \mathbf{N}_e(t) dx' = \frac{\mu l_e}{6} \begin{bmatrix} 2 & 0 & 0 & 1 & 0 & 0 \\ 0 & 2 & 0 & 0 & 1 & 0 \\ 0 & 0 & 2 & 0 & 0 & 1 \\ 1 & 0 & 0 & 2 & 0 & 0 \\ 0 & 1 & 0 & 0 & 2 & 0 \\ 0 & 0 & 1 & 0 & 0 & 2 \end{bmatrix} \tag{4.35}$$

$$\mathbf{K}'_e = \frac{1}{l_e} \begin{bmatrix} AE & 0 & 0 & -AE & 0 & 0 \\ 0 & F_0 & 0 & 0 & -F_0 & 0 \\ 0 & 0 & F_0 & 0 & 0 & -F_0 \\ -AE & 0 & 0 & AE & 0 & 0 \\ 0 & -F_0 & 0 & 0 & F_0 & 0 \\ 0 & 0 & -F_0 & 0 & 0 & F_0 \end{bmatrix} \tag{4.36}$$

$$\mathbf{p}'_e(t) = \int_0^{l_e} \mathbf{N}^T(x') \mathbf{p}'_e(x',t) dx' = \begin{bmatrix} \int_0^{l_e} N_1(x') p'_{x'}(x',t) dx' \\ \int_0^{l_e} N_1(x') p'_{y'}(x',t) dx' \\ \int_0^{l_e} N_1(x') p'_{z'}(x',t) dx' \\ \int_0^{l_e} N_2(x') p'_{x'}(x',t) dx' \\ \int_0^{l_e} N_2(x') p'_{y'}(x',t) dx' \\ \int_0^{l_e} N_2(x') p'_{z'}(x',t) dx' \end{bmatrix} = \frac{l}{2} \begin{bmatrix} p'_{x'}(t) \\ p'_{y'}(t) \\ p'_{z'}(t) \\ p'_{x'}(t) \\ p'_{y'}(t) \\ p'_{z'}(t) \end{bmatrix} \tag{4.37}$$

In the final result of (4.37) it has been assumed that the loads per unit length are constant within the element. The Lagrange equations of motion of one element can now be written as

$$\begin{aligned} &\frac{d}{dt}\left(\frac{\partial l_e}{\partial \dot{\mathbf{q}}_e^T} \right) - \frac{\partial l_e}{\partial \mathbf{q}_e^T} = -\mathbf{C}'_e \dot{\mathbf{q}}'_e \Rightarrow \\ &\mathbf{M}'_e \ddot{\mathbf{q}}'_e + \mathbf{C}'_e \dot{\mathbf{q}}'_e + \mathbf{K}'_e \mathbf{q}'_e = \mathbf{p}'_e(t) + \mathbf{r}'_e(t) \end{aligned} \tag{4.38}$$

$\mathbf{C}'_e$ is the linear viscous element damping matrix. The damping matrix is assumed to be proportional to the mass- and stiffness matrices, i.e. Rayleigh damping

$$\mathbf{C}'_e = a_0 \mathbf{M}'_e + a_1 \mathbf{K}'_e \tag{4.39}$$

The two damping coefficients a_0 and a_1 are determined from the corresponding global structural damping matrix as indicated in the following.

4.2.1 Cable equation of motion

The equation of motion of one element in the global (X,Y,Z)-coordinate system may be written as

$$\mathbf{M}_e\ddot{\mathbf{q}}_e+\mathbf{C}_e\dot{\mathbf{q}}_e+\mathbf{K}_e\mathbf{q}_e=\mathbf{p}_e(t)+\mathbf{r}_e(t) \tag{4.40}$$

The transformation between local and global components of the DOF-vector may be written as

$$\mathbf{q}_e(t)=\mathbf{A}_e\mathbf{q}'_e(t) \tag{4.41}$$

The corresponding transformation between local and global components of the element matrices, load and reaction vectors read

$$\mathbf{M}_e=\mathbf{A}_e^T\mathbf{M}'_e\mathbf{A}_e \quad , \quad \mathbf{C}_e=\mathbf{A}_e^T\mathbf{C}'_e\mathbf{A}_e \quad , \quad \mathbf{K}_e=\mathbf{A}_e^T\mathbf{K}'_e\mathbf{A}_e \tag{4.42}$$

$$\mathbf{p}_e(t)=\mathbf{A}_e^T\mathbf{p}'_e(t) \quad , \quad \mathbf{r}_e(t)=\mathbf{A}_e^T\mathbf{r}'_e(t) \tag{4.43}$$

The transformation matrix $\mathbf{A}_e$ is given by

$$\mathbf{A}_e=\begin{bmatrix}\mathbf{A}_{0e} & \mathbf{0}\\ \mathbf{0} & \mathbf{A}_{0e}\end{bmatrix} \quad , \quad \mathbf{A}_{0e}=\begin{bmatrix}\cos\varphi_e & -\sin\varphi_e & 0\\ \sin\varphi_e & \cos\varphi_e & 0\\ 0 & 0 & 1\end{bmatrix} \tag{4.44}$$

Assembling all element matrices and correction for kinematic boundary conditions leads to the global equation of motion

$$\underset{mxm}{\mathbf{M}_S}\,\underset{mx1}{\ddot{\mathbf{v}}_S}+\underset{mxm}{\mathbf{C}_S}\,\underset{mx1}{\dot{\mathbf{v}}_S}+\underset{mxm}{\mathbf{K}_S}\,\underset{mx1}{\mathbf{v}_S}=\underset{mx1}{\mathbf{p}_S}\left(\boldsymbol{\theta}_S,\dot{\mathbf{v}}_S\right) \tag{4.45}$$

where $\mathbf{v_S}=\mathbf{v_S}(t)$, $\dot{\mathbf{v}}_\mathbf{S}=\dot{\mathbf{v}}_\mathbf{S}(t)$, and $\ddot{\mathbf{v}}_\mathbf{S}=\ddot{\mathbf{v}}_\mathbf{S}(t)$ denotes the time dependent systems displacement-, velocity-, and acceleration vector in the global (X,Y,Z) coordinate system, respectively and $\mathbf{M}_S$, $\mathbf{C}_S$, and $\mathbf{K}_S$ are the structural mass-, damping-, and stiffness matrices, respectively. According to (4.39), a_0 and a_1 are determined so the damping matrix represents the 1st and 2nd in-plane modal damping ratios ζ_1 and ζ_2 correct. This implies the calibration, (Nielsen, 2004)

$$\begin{bmatrix}a_0\\ a_1\end{bmatrix}=\frac{2\omega_1\omega_2}{\omega_2^2-\omega_1^2}\begin{bmatrix}\omega_2 & -\omega_1\\ -\dfrac{1}{\omega_2} & \dfrac{1}{\omega_1}\end{bmatrix}\begin{bmatrix}\zeta_1\\ \zeta_2\end{bmatrix} \tag{4.46}$$

where ω_1 and ω_2 denotes the undamped angular frequencies of the two lowest in-plane eigenmodes, and ζ_1 and ζ_2 are the corresponding modal damping ratios, which are assumed to be known.

The contribution to $\mathbf{p}_\mathrm{S}(t)$ from self-induced aerodynamic loads are described in section 4.1. Only loads in the y'-direction is considered. Hence, loads in the local x'-direction (chord-wise) and the local z'-direction (out-of-plane) are ignored. According to (4.18), the load per unit length may be expressed as follows

$$p_{y',e}\left(\theta_e,\dot{v}_{y',e}\right)=p_{y',0}+p_{y',1}\dot{v}_{y',e}+p_{y',2}\theta_e \tag{4.47}$$

where $\theta_e=\theta_e(t)$ is the centre angle describing the dynamic position of the rivulet which is assumed constant along the cable finite element, c.f. section 4.1. The three components in (4.47) specifies a quasi-static contribution, an aerodynamic viscous damping term, and an aerodynamic stiffness term, respectively. On matrix form and expressed in global coordinates they are written as follows

$$\underset{mx1}{\mathbf{p}_S}\left(\boldsymbol{\theta}_S,\dot{\mathbf{v}}_S\right)=\underset{mxn\ nx1}{\mathbf{K}_1}\,\boldsymbol{\theta}_S+\underset{mxm\ mx1}{\mathbf{C}_1}\,\dot{\mathbf{v}}_S+\underset{mx1}{\mathbf{p}_0} \tag{4.48}$$

where

$$\boldsymbol{\theta}_S(t)=\begin{bmatrix}\theta_1(t)\\ \vdots \\ \theta_n(t)\end{bmatrix} \quad , \quad \mathbf{v}_S(t)=\begin{bmatrix}v_1(t)\\ \vdots \\ v_m(t)\end{bmatrix} \tag{4.49}$$

$$\mathbf{K}_1=-\frac{1}{2}\begin{bmatrix}\mathbf{k}_1 & \mathbf{k}_2 & 0 & 0 & 0\\ 0 & \mathbf{k}_2 & \mathbf{k}_3 & \ddots & \vdots \\ 0 & 0 & \mathbf{k}_3 & \ddots & 0\\ 0 & \ddots & \ddots & \ddots & \mathbf{k}_n\\ 0 & \cdots & 0 & 0 & \mathbf{k}_n\end{bmatrix}, \mathbf{k}_i=l_{e,i}p_{y',2}\begin{bmatrix}-\sin\varphi_i\\ \cos\varphi_i\\ 0\end{bmatrix} \tag{4.50}$$

$$\mathbf{C}_1=\frac{1}{4}\begin{bmatrix}\mathbf{c}_1 & \mathbf{c}_2 & 0 & 0 & 0\\ 0 & \mathbf{c}_2 & \mathbf{c}_3 & \ddots & \vdots \\ 0 & 0 & \mathbf{c}_3 & \ddots & 0\\ 0 & \ddots & \ddots & \ddots & \mathbf{c}_n\\ 0 & \cdots & 0 & 0 & \mathbf{c}_n\end{bmatrix}, \mathbf{c}_i=l_{e,i}p_{y',1}\begin{bmatrix}\sin^2\varphi_i & -\sin\varphi_i\cos\varphi_i & 0\\ -\sin\varphi_i\cos\varphi_i & \cos^2\varphi_i & 0\\ 0 & 0 & 0\end{bmatrix} \tag{4.51}$$

$$\mathbf{p}_0=\frac{1}{2}\begin{bmatrix}\mathbf{p}_{0,1}\\ \mathbf{p}_{0,2}+\mathbf{p}_{0,1}\\ \vdots \\ \mathbf{p}_{0,m-1}+\mathbf{p}_{0,m-2}\\ \mathbf{p}_{0,m}\end{bmatrix}, \mathbf{p}_{0,i}=l_{e,i}p_{y',0}\begin{bmatrix}-\sin\varphi_i\\ \cos\varphi_i\\ 0\end{bmatrix} \tag{4.52}$$

It should be noted that the $\mathbf{C_1}$ contributions are computed by the displacements defined in (4.29) which is the mean of the displacements in each node.

4.2.2 Rivulet equation of motion

The equation of motion of the rivulet will be generated by use of an analytical model similar to the Robra model, c.f. section 2.1. The oscillation of the rivulet will in nature behave differently along the cable, but in the numerical model it is assumed to oscillate in a uniform way along each finite element. Hence, no coupling of the rivulet motion between adjacent elements. However, as will be accounted for below, the rivulet motion merely depends on the cable motion which in turn introduces a connection of the rivulet motion between adjacent elements. The SDOF representation of the rivulet model is illustrated in figure 18.

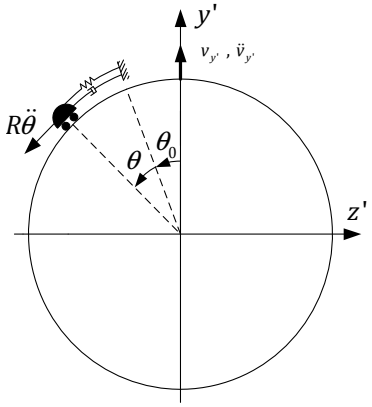

Figure 18: Excitation mechanism and SDOF model of the rivulet motion.

When θ_0 is imposed a small perturbation θ, the rivulets will perform damped eigenvibrations around θ_0 specified by the undamped angular eigenfrequency ω_r and a non-linear damping mechanism indicated below. Results from wind tunnel tests indicate that the frequency of the rivulet motion is almost the same as that of the cable motion when rain/wind induced vibrations take place, (Hikami, et al., 1988). In the numerical model $\omega_r = \omega_c$ will be used, where ω_c signifies the fundamental frequency of the cable model.

The motion of the rivulet is caused by the tangential acceleration $-\ddot{v}_{y'} sin(\theta + \theta_0)$ of the cable at the position of the rivulet in the direction defined by the DOF θ.

The dynamic equation of motion for the rivulet follows by application of Newton's 2nd law of motion to rivulet mass m, (Wang, et al., 2003). A linearization around θ_0 has been introduced in consistence with the previous approximations.

$$\begin{aligned} & m\left(R\ddot{\theta} + 2\zeta_r\omega_r\left|\dot{\theta}\right|^{a_r} R\dot{\theta} + \omega_r^2 R\theta\right) = m\ddot{v}_{y'}\sin\left(\theta_0 + \theta\right) \\ & \Downarrow \\ & \ddot{\theta} + 2\zeta_r\omega_r\left|\dot{\theta}\right|^{a_r}\dot{\theta} + \omega_r^2\theta = \frac{\ddot{v}_{y'}}{R}\left(\sin\theta_0 + \cos\left(\theta_0\right)\theta\right) \end{aligned} \tag{4.53}$$

where ζ_r is a non-dimensional damping parameter which is assumed to be known. Based on the achieved literature $\zeta_r = 10$, (Wang, et al., 2003). The parameter a_r is in the interval $a_r \in [0,1]$ which means that the damping model may be envisioned as an interpolation between a linear viscous damping model $(a_r = 0)$ and a fluid damping model $(a_r = 1)$.

The equations of motion for the n number of rivulets are assembled in the matrix equation

$$\underset{nx1}{\ddot{\boldsymbol{\theta}}_S} + \underset{nxn}{\mathbf{C}_2\left(\dot{\boldsymbol{\theta}}_S\right)}\underset{nx1}{\boldsymbol{\theta}_S} + \underset{nxn}{\mathbf{K}_2}\underset{nx1}{\boldsymbol{\theta}_S} - \underset{nxm}{\mathbf{M}_1\left(\boldsymbol{\theta}_S\right)}\underset{mx1}{\ddot{\mathbf{v}}_S} = \underset{nx1}{\mathbf{0}} \tag{4.54}$$

where

$$\mathbf{C}_2\left(\dot{\boldsymbol{\theta}}_S\right) = 2\zeta_r\omega_r\begin{bmatrix} \left|\dot{\theta}_1\right|^{a_r} & 0 & 0 \\ 0 & \ddots & 0 \\ 0 & 0 & \left|\dot{\theta}_n\right|^{a_r} \end{bmatrix},\ \mathbf{M}_1\left(\boldsymbol{\theta}_S\right) = \frac{1}{R}\begin{bmatrix} \sin\theta_0 + \theta_1\cos\theta_0 & \mathbf{a}_1^T \\ \vdots & \vdots \\ \sin\theta_0 + \theta_n\cos\theta_0 & \mathbf{a}_n^T \end{bmatrix},\ \mathbf{K}_2 = \omega_r^2\mathbf{I} \tag{4.55}$$

The constants ω_r, ζ_r, and a_r are assumed to be the same for all cable finite elements and the transformation vector $\mathbf{a}_i^T$ is defined by

$$v_{y,i} = \underset{1xmmx1}{\mathbf{a}_i^T\,\mathbf{v}_S} \qquad \mathbf{a}_i^T = \begin{bmatrix} 0 & \cdots & 0 & -\sin\varphi_i & \cos\varphi_i & 0 & \cdots & 0 \end{bmatrix} \tag{4.56}$$

As mentioned, the linearized approximations require that the dynamic increment fulfils $|\Delta\theta| \ll 1$ when θ is measured in radians. This has been accounted for in the numerical model as the computations will stop if the condition is violated.

4.2.3 Linearization of the rivulet damping term

When the pole placement method is applied, c.f. section 4.3.3, the coefficient matrix $\mathbf{A}$ must be constant. An equivalent damping parameter $\zeta_{r,e}$ of the rivulet oscillator is therefore sought.

The nonlinear damping force f_d on the rivulet from (4.53) reads

$$f_d = 2\zeta_r\omega_r\left|\dot{\theta}\right|^{a_r}\dot{\theta} \tag{4.57}$$

The linearization must satisfy an equal energy dissipation per period T_r, which results in the following

$$\int_0^{T_r} f_d(t)\dot{\theta}(t)dt = \int_0^{T_r} 2\zeta_r \omega_r \left|\dot{\theta}\right|^{a_r} \dot{\theta}^2 dt = \int_0^{T_r} 2\zeta_{r,e}\omega_r \dot{\theta} dt \tag{4.58}$$

where $\zeta_{r,e}$ is the equivalent damping ratio. Isolation of $\zeta_{r,e}$ yields

$$\zeta_{r,e} = \zeta_r \frac{\int_0^{T_r} \left|\dot{\theta}\right|^{a_r} \theta dt}{\int_0^{T_r} \dot{\theta}^2 dt} \tag{4.59}$$

A harmonic oscillation is assumed with the period $\omega_r t$ and the amplitude θ_{amp}

$$\theta(t) = \theta_{amp}\cos(\omega_r t) \Rightarrow \dot{\theta}(t) = -\theta_{amp}\omega_r \sin(\omega_r t) \tag{4.60}$$

If (4.60) is inserted in (4.59) the following expression for $\zeta_{r,e}$ appear

$$\begin{aligned}\zeta_{r,e} &= \zeta_r \frac{\omega_r \int_0^{2\pi} \left(\theta_{amp}\omega_r\right)^2 \sin^2\tau \left(\theta_{amp}\omega_r\right)^{a_r} \left|\sin\tau\right|^{a_r} d\tau}{\omega_r \int_0^{2\pi} \left(\theta_{amp}\omega_r\right)^2 \sin^2\tau d\tau} \\ &= \zeta_r \left(\theta_{amp}\omega_r\right)^{a_r} \underbrace{\frac{4}{\pi}\int_0^{\frac{\pi}{2}} \sin^2\tau \left|\sin\tau\right|^{a_r} d\tau}_{f(a_r)}\end{aligned} \tag{4.61}$$

where $\tau = \omega_r t = \frac{2\pi}{T_r}$. Substituting $y = \cos t$ and solving $f(a_r)$ numerically, yields

$$\begin{aligned} f(a_r) &= \frac{4}{\pi}\int_0^{\frac{\pi}{2}} \sin^2\tau \left|\sin^2\tau\right| d\tau \\ &= \frac{4}{\pi}\int_0^1 \left(1-y^2\right)^{\frac{1+a_r}{2}} dy \\ &= \begin{cases} 1\,, a_r = 0 \\ 0.93\,, a_r = 0.4 \\ 0.92\,, a_r = 0.5 \\ 0.85\,, a_r = 1 \end{cases} \end{aligned} \tag{4.62}$$

The parameter a_r is chosen in accordance with (Wang, et al., 2003). Wind tunnel tests have indicated rivulet amplitudes of $\theta_{amp} = 10° \approx 0.17rad$, (Hikami, et al., 1988). It must be noted that this value entail some uncertainty. The rivulet damping ratio $\zeta_r = 10$ and the undamped angular eigenfrequency of the rivulet $\omega_r \approx \omega_c = 2.37s^{-1}$. The general expression of $\zeta_{r,e}$ reads

$$\begin{aligned} \zeta_{r,e} &= \zeta_r \left(\theta_{amp}\omega_r\right)^{a_r} f(a_r) \\ &= 10\left(0.17 \cdot 2.37\right)^{a_r} f(a_r) \\ &= \begin{cases} 10\ , \ a_r = 0 \\ 6.46\ , \ a_r = 0.4 \\ 5.84\ , \ a_r = 0.5 \\ 3.42\ , \ a_r = 1 \end{cases} \end{aligned} \tag{4.63}$$

4.2.4 State vector formulation

The expressions (4.45), (4.48) and (4.54) may be assembled in the following global nonlinear equation of motion describing the coupled cable-rivulet system

$$\begin{array}{ccccccccc} \mathbf{M}_S\ddot{\mathbf{v}}_S & + & (\mathbf{C}_S-\mathbf{C}_1)\dot{\mathbf{v}}_S & + & \mathbf{K}_S\mathbf{v}_S-\mathbf{K}_1\boldsymbol{\theta}_S & - & \mathbf{p}_0 & = & \mathbf{0} \\ \underbrace{-\mathbf{M}_1(\boldsymbol{\theta}_S)\ddot{\mathbf{v}}_S+\ddot{\boldsymbol{\theta}}_S}_{Mass\,contribution} & + & \underbrace{\mathbf{C}_2(\dot{\boldsymbol{\theta}}_S)\dot{\boldsymbol{\theta}}_S}_{Damping\,contribution} & + & \underbrace{\mathbf{K}_2\boldsymbol{\theta}_S}_{Stiffness\,contribution} & & \underbrace{\quad}_{Load\ contribution} & = & \mathbf{0} \end{array} \tag{4.64}$$

which may be expressed on matrix form as

$$\mathbf{M}(\boldsymbol{\theta}_S)\ddot{\mathbf{w}}(t)+\mathbf{C}(\dot{\boldsymbol{\theta}}_S)\dot{\mathbf{w}}(t)+\mathbf{K}\mathbf{w}(t)=\mathbf{p}\ \ ,\ \ t>0 \tag{4.65}$$

The introduced matrices in (4.65) are defined as

$$\begin{aligned} \underset{(m+n)x(m+n)}{\mathbf{M}(\boldsymbol{\theta}_S)} &= \begin{bmatrix} \mathbf{M}_S & \mathbf{0} \\ -\mathbf{M}_1(\boldsymbol{\theta}_S) & \mathbf{I} \end{bmatrix} \qquad \underset{(m+n)x1}{\mathbf{p}} = \begin{bmatrix} \mathbf{p}_0 \\ \mathbf{0} \end{bmatrix} \\ \underset{(m+n)x(m+n)}{\mathbf{C}(\dot{\boldsymbol{\theta}}_S)} &= \begin{bmatrix} \mathbf{C}_S-\mathbf{C}_1 & \mathbf{0} \\ \mathbf{0} & \mathbf{C}_2(\dot{\boldsymbol{\theta}}_S) \end{bmatrix} \quad \underset{(m+n)x1}{\mathbf{w}(t)} = \begin{bmatrix} \mathbf{v}_S(t) \\ \boldsymbol{\theta}_S(t) \end{bmatrix} \\ \underset{(m+n)x(m+n)}{\mathbf{K}} &= \begin{bmatrix} \mathbf{K}_S & -\mathbf{K}_1 \\ \mathbf{0} & \mathbf{K}_2 \end{bmatrix} \end{aligned} \tag{4.66}$$

The time-varying ordinary differential equation (4.64) is solved with respect to the initial conditions $\mathbf{w}(0)=\mathbf{w}_0$ and $\dot{\mathbf{w}}(0)=\dot{\mathbf{w}}_0$, by means of numerical integration. In the present case this is done by explicit integration where the fourth order Runge-Kutta method (RK4) is applied. Then, (4.64) must be expressed on the state vector form. (4.65) may be written as

$$\begin{bmatrix} \dot{\mathbf{w}}(t) \\ \ddot{\mathbf{w}}(t) \end{bmatrix} = \begin{bmatrix} \mathbf{0} & \mathbf{I} \\ -\mathbf{M}^{-1}(\boldsymbol{\theta}_S)\mathbf{K} & -\mathbf{M}^{-1}(\boldsymbol{\theta}_S)\mathbf{C}(\dot{\boldsymbol{\theta}}_S) \end{bmatrix} \begin{bmatrix} \mathbf{w}(t) \\ \dot{\mathbf{w}}(t) \end{bmatrix} + \begin{bmatrix} \mathbf{0} \\ \mathbf{M}^{-1}(\boldsymbol{\theta}_S)\mathbf{p} \end{bmatrix} \tag{4.67}$$

which may be written as the following state vector formulation

$$\begin{aligned} &\dot{\mathbf{z}}(t)=\mathbf{A}(\boldsymbol{\theta}_S,\dot{\boldsymbol{\theta}}_S)\mathbf{z}(t)+\mathbf{b}_0(\boldsymbol{\theta}_S)\ \ ,\ \ t>0 \\ &\mathbf{z}(0)=\mathbf{z}_0 \end{aligned} \tag{4.68}$$

where the introduced matrices in the latter expression are defined as

$$\mathbf{z}(t)=\begin{bmatrix} \mathbf{w}(t) \\ \dot{\mathbf{w}}(t) \end{bmatrix}\ \ ,\ \ \mathbf{z}_0=\begin{bmatrix} \mathbf{w}_0 \\ \dot{\mathbf{w}}_0 \end{bmatrix} \tag{4.69}$$

$$\begin{aligned} \mathbf{A}(\boldsymbol{\theta}_S,\dot{\boldsymbol{\theta}}_S) &= \begin{bmatrix} \mathbf{0} & \mathbf{I} \\ -\mathbf{M}^{-1}(\boldsymbol{\theta}_S)\mathbf{K} & -\mathbf{M}^{-1}(\boldsymbol{\theta}_S)\mathbf{C}(\dot{\boldsymbol{\theta}}_S) \end{bmatrix} \\ \mathbf{b}_0(\boldsymbol{\theta}_S) &= \begin{bmatrix} \mathbf{0} \\ \mathbf{M}^{-1}(\boldsymbol{\theta}_S)\mathbf{p} \end{bmatrix} \end{aligned} \tag{4.70}$$

The inverse of the mass matrix is given as

$$\mathbf{M}^{-1}(\boldsymbol{\theta}_S)=\begin{bmatrix} \mathbf{M}_S^{-1} & \mathbf{0} \\ \mathbf{M}(\boldsymbol{\theta}_S)\mathbf{M}_S^{-1} & \mathbf{I} \end{bmatrix} \tag{4.71}$$

The RK4 method, according to (4.72), may be used to evaluate $\mathbf{z}(t_{n+1})$.

$$\begin{aligned}
\mathbf{z}_{n+1} &= \mathbf{z}_n + \frac{\Delta t}{6}\left(\mathbf{k}_1 + 2\mathbf{k}_2 + 2\mathbf{k}_3 + \mathbf{k}_4\right) \\
\mathbf{k}_1 &= f\left(\mathbf{z}_n\right) \\
\mathbf{k}_2 &= f\left(\mathbf{z}_n + 0.5\Delta t\mathbf{k}_1\right) \\
\mathbf{k}_3 &= f\left(\mathbf{z}_n + 0.5\Delta t\mathbf{k}_2\right) \\
\mathbf{k}_4 &= f\left(\mathbf{z}_n + \Delta t\mathbf{k}_3\right)
\end{aligned} \tag{4.72}$$

where Δt is the time step and $f(\mathbf{z})$ denotes the right hand side of (4.72). The implementation of the damping mechanisms described in chapter 3 will be treated consequently.

4.3 Control Algorithms

Introducing a damper force leads to an expansion of the state vector formulation (4.68). In collocated feedback control the control force depends on the response of the damper node only. In state feedback control the control force depends on the state of the system, which in the present case is described by the state vector $\mathbf{z}(t)$. In the following sections, the control algorithms used in the numerical model will be described. The perpendicularly attached dampers are handled initially, followed by the active control of axial forces.

The cable, the position of the perpendicularly attached damper (as introduced in chapter 3), and the related variables are illustrated in figure 19. The damper is attached to node i, which has the displacement vector $\mathbf{v}_i$ with the global components v_{3i-2}, v_{3i-1}, and v_{3i} in the global (X,Y,Z)-coordinate system. The unit vector $\mathbf{n}$ is used to signify the direction of the damper force $u(t)$. The derivation of the global control force for the perpendicularly attached dampers is descried consequently.

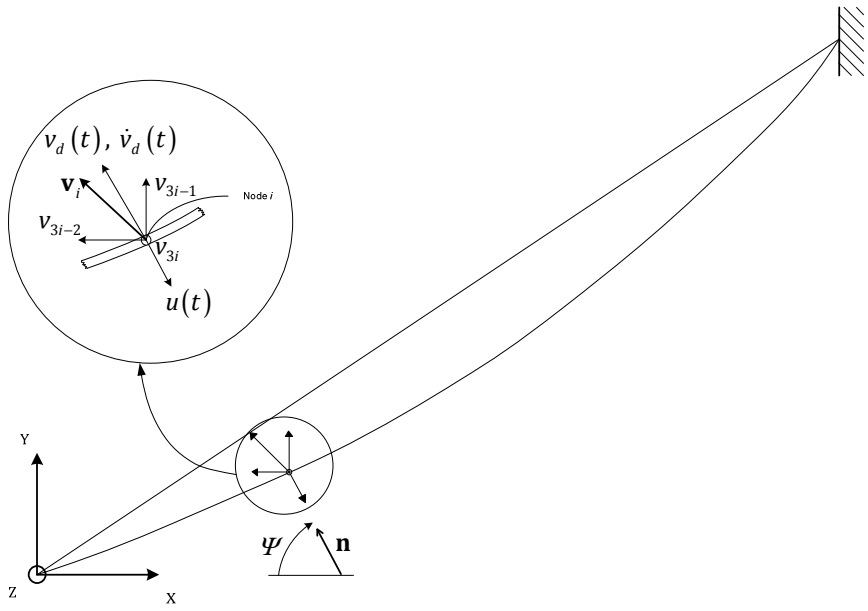

Figure 19: Control forces on the cable in the dynamic state.

The damper is placed in the (X,Y)-plane and has the inclination Ψ with the X-axis. Then, the displacement v_d and the velocity $\dot{v}_d$ of the damper support point in the direction of $\mathbf{n}$ are given as

$$v_d(t) = \mathbf{n}^T\mathbf{v}_i(t) \quad , \quad \dot{v}_d(t) = \mathbf{n}^T\dot{\mathbf{v}}_i(t) \quad , \quad \mathbf{n}^T = \begin{bmatrix} -\cos\Psi & \sin\Psi & 0 \end{bmatrix} \tag{4.73}$$

Formally, the nodal displacement vector corresponding to node i can be written in terms of the global system displacement vector by means of the following transformation

$$\mathbf{v}_i(t)=\mathbf{A}_i\mathbf{v}_S(t) \quad , \quad \mathbf{v}_S(t)=\begin{bmatrix}\mathbf{v}_1(t)\\ \mathbf{v}_2(t)\\ \vdots\\ \mathbf{v}_i(t)\\ \vdots\\ \mathbf{v}_{n-1}(t)\end{bmatrix} \quad , \quad \underset{3xm}{\mathbf{A}_i}=\begin{bmatrix}\mathbf{0} & \mathbf{0} & \cdots & \underset{3\times3}{\mathbf{I}} & \cdots & \mathbf{0}\end{bmatrix} \tag{4.74}$$

The control force must be expressed in terms of components related to the global coordinate system. The control force on node i has the magnitude $u(t)$ and is opposite directed to $\mathbf{n}$. Then, the global control force vector $\mathbf{p}_c(t)$ of dimension $mx1$ may be expressed as

$$\mathbf{p}_c(t)=-\mathbf{A}_i^T\mathbf{n}u(t) \tag{4.75}$$

$\mathbf{p}_c(t)$ is added to the static aerodynamic load in (4.65). Then, (4.65) may be written as

$$\mathbf{M}(\boldsymbol{\theta}_S)\ddot{\mathbf{w}}(t)+\mathbf{C}(\dot{\boldsymbol{\theta}}_S)\dot{\mathbf{w}}(t)+\mathbf{K}\mathbf{w}(t)=\mathbf{p}+\mathbf{p}_1u(t) \ , \ t>0 \tag{4.76}$$

where

$$\underset{(m+n)x1}{\mathbf{p}_1}=\begin{bmatrix}-\mathbf{A}_i^T\mathbf{n}\\ \mathbf{0}\end{bmatrix} \tag{4.77}$$

Then, (4.68) may be recasted as follows

$$\dot{\mathbf{z}}(t)=\mathbf{A}(\boldsymbol{\theta}_S,\dot{\boldsymbol{\theta}}_S)\mathbf{z}(t)+\mathbf{b}_0(\boldsymbol{\theta}_S)+\mathbf{b}(\boldsymbol{\theta}_S)u(t) \ , \ t>0 \tag{4.78}$$

where

$$\mathbf{b}(\boldsymbol{\theta}_S)=\begin{bmatrix}\mathbf{0}\\ \mathbf{M}^{-1}(\boldsymbol{\theta}_S)\mathbf{p}_1\end{bmatrix} \tag{4.79}$$

Using (4.71) and (4.77) the matrix product $\mathbf{M}^{-1}(\boldsymbol{\theta}_S)\mathbf{p_1}$ may be evaluated as

$$\mathbf{M}^{-1}(\boldsymbol{\theta}_S)\mathbf{p}_1=-\begin{bmatrix}\mathbf{I}\\ \mathbf{M}_1(\boldsymbol{\theta}_S)\end{bmatrix}\mathbf{M}_S^{-1}\mathbf{A}_i^T\mathbf{n} \tag{4.80}$$

The following sections will give specifications for $u(t)$ in accordance to the considered damping mechanism. The global control force vector $\mathbf{p}_c(t)$ will be expressed according to each of the control laws.

4.3.1 Passive viscous damping

The co-reaction force $u(t)$ induced by the viscous damper is given by the expression

$$u(t)=c\dot{v}_d(t) \tag{4.81}$$

where c is the damping coefficient fitted to the cable characteristics. The damping coefficient in case of optimal tuning to the nth mode is given by the following expressions on the condition that the damper is acting in the orthogonal direction to the cable chord, (Krenk, 2000),(Kovacs, 1982).

$$c_{opt}=\sqrt{F_0\mu}\frac{1}{n\pi\frac{a}{L}} \tag{4.82}$$

The optimal damping ratio becomes

$$\zeta_{opt} \simeq \frac{a}{2L} \tag{4.83}$$

If the tuning is performed to the 1st mode $\zeta_1 = \zeta_{opt}$, the modal damping ratio of the higher modes are approximately given as, (Krenk, 2000)

$$\zeta_n \simeq \zeta_{opt} \frac{2n}{1+n^2} \tag{4.84}$$

The global control force distribution vector according to (4.75) for the viscous damper can be written as

$$\begin{aligned} u(t) &= c\dot{v}_d(t) = c\mathbf{n}^T \dot{\mathbf{v}}_i(t) = c\mathbf{n}^T \mathbf{A}_i \dot{\mathbf{v}}_S(t) \Rightarrow \\ \mathbf{p}_c(t) &= -c\mathbf{A}_i^T \mathbf{n}\mathbf{n}^T \mathbf{A}_i \dot{\mathbf{v}}_S(t) \end{aligned} \tag{4.85}$$

4.3.2 Semi active MR-damping

The MR damper is considered as a combined variable linear viscous and friction damper. The friction part of the model has for long been described by the Bouc-Wen model, which has been rather accurate, (Zhou, et al., 2006). However, the number of parameters to be identified in this model is up to 14, which can make it quite impractical. As the well known Coulomb friction model does not rightfully represent the force-velocity relationship in the low-velocity range, neither this model should be used. Instead, *Zhou, Nielsen* and *Qu* suggested a modified Dahl hysteresis model as illustrated in figure 20, based on experimental results, (Zhou, et al., 2006). This model has proved good accuracy, reduces the amount of unidentified parameters to 8, and it is valid in the low-velocity range. The model basis is that the friction force is only position dependent, as it is only a function of the dynamic cable displacement and sign of cable velocity.

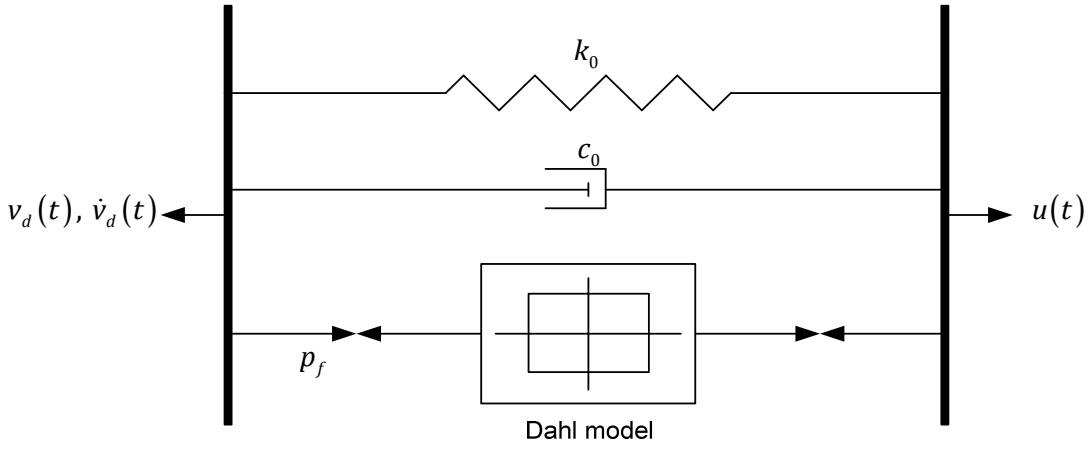

Figure 20: Modified Dahl model of the MR damper.

The control force is given by

$$u(t) = k_0 v_d(t) + c_0 \dot{v}_d(t) + p_f(t) z(t) - p_0 \tag{4.86}$$

where k_0 is the linear stiffness coefficient, c_0 is the variable viscous damping coefficient, p_f is the friction force modulated by the applied magnetic field, and p_0 is a damper force caused by seals and measurement bias. z is a hysteretic variable which describes the following hysteresis relation between the friction force and the cable velocity

$$\dot{z}(t) = \sigma \dot{v}_d(t)\left(1 - \operatorname{sgn}\left(\dot{v}_d(t)\right) z(t)\right) \tag{4.87}$$

where σ characterize the hysteretic loop shape. When the fluctuating magnetic field is applied, the Dahl model should be calibrated. This is done through the parameters c_0 and p_f, which depend on the applied magnetic field.

$$c_0(t) = c_{0,0} + c_{0,1} y(t) \tag{4.88}$$

$$p_f(t) = p_{f,0} + p_{f,1} y(t) \tag{4.89}$$

where $c_{0,0}$ is the damping coefficient corresponding to the damping coefficient of an equivalent linear viscous damper and $p_{f,0}$ is the Coulomb force of the MR-damper when the applied voltage $V = 0V$. y is an intrinsic variable in the model, which is determined by the first-order filter

$$\dot{y}(t) = -\eta\big(y(t) - V\big) \tag{4.90}$$

η describes the response time of the MR-damper. The larger η, the smaller response time. When η is large, $y \approx V$, which when inserted in (4.89) gives the following expression for the needed voltage

$$V_{need} = \frac{p_f(t) - p_{f,0}}{p_{f,1}} \tag{4.91}$$

The control demand for the friction force p_f is proportional to the absolute value of the previous peak extremum of $v_d(t)$ determined by the functional P as illustrated in figure 21.

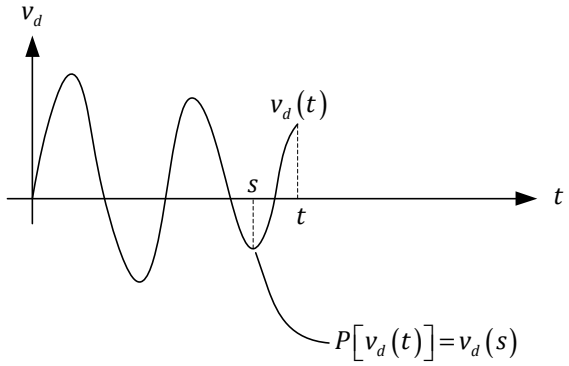

Figure 21: Peak determination.

Consider the formulation

$$p_f(t) = p_{f,0} + p_{f,1} y(t) = \beta_f \left| P\left[v_d(t)\right] \right| \tag{4.92}$$

where β_f is a controller gain adjusted to the considered system. If (4.92) is inserted in (4.91), V_{need} can be found by

$$V_{need}(t) = \frac{\beta_f \left| P\left[v_d(t)\right] \right| - p_{f,0}}{p_{f,1}} \tag{4.93}$$

The applied voltage to the MR-damper is given on the form

$$V(t) = \begin{cases} 0 & , \; V_{need}(t) \le 0 \\ V_{need}(t) & , \; 0 \le V_{need}(t) \le V_{\max} \\ V_{\max} & , \; V_{need}(t) \ge V_{\max} \end{cases} \tag{4.94}$$

An important merit is the easy implementation as only the local dynamic responses $v_d(t)$ and $\dot{v}_d(t)$ are needed. However, the optimal controller gain β_f is unknown and should be estimated by numerical trials.

Inserting (4.86) in (4.75) gives the global control force distribution vector for the semi-active MR-damper as

$$\mathbf{p}_c(t) = -\mathbf{A}_i^T \mathbf{n}\mathbf{n}^T \mathbf{A}_i \left(k_0 \mathbf{v}_S(t) + c_0 \dot{\mathbf{v}}_S(t)\right) - \mathbf{A}_i^T \mathbf{n}\left(p_f z - p_0\right) \tag{4.95}$$

4.3.3 Active control by pole placement

In the active state feedback control the first $2N_1$ closed loop poles associated with the first $2N_1$ closed loop eigenmodes are prescribed, where $N_1 < N$ and $N = m + n$. The state feedback controller gain vector $\mathbf{g}_{PP}$ of dimension $2Nx1$, which produce the addressed closed loop poles are determined by the pole placement method presented below. For a single input system, the control force may be written as

$$u(t) = \mathbf{g}_{PP}^T \mathbf{z}(t) \tag{4.96}$$

(4.96) is inserted in the state vector formulation (4.78)

$$\dot{\mathbf{z}}(t) = \overline{\mathbf{A}}\mathbf{z}(t) + \mathbf{b}_0 \tag{4.97}$$

where

$$\overline{\mathbf{A}} = \mathbf{A} + \mathbf{b}\mathbf{g}_{PP}^T \tag{4.98}$$

where $\overline{\mathbf{A}} = \overline{\mathbf{A}}(\boldsymbol{\theta}_S, \dot{\boldsymbol{\theta}}_S)$, $\mathbf{A} = \mathbf{A}(\boldsymbol{\theta}_S, \dot{\boldsymbol{\theta}}_S)$, $\mathbf{b}_0 = \mathbf{b}_0(\boldsymbol{\theta}_S)$, and $\mathbf{b} = \mathbf{b}(\boldsymbol{\theta}_S)$. In a practical implementation of the algorithm the system state vector $\mathbf{z}(t)$ must be estimated by a state observer equation, (Juang, et al., 2001). Normally, only the cable displacements can be measured. Hence, it may be questioned whether the part of the state vector defining the rivulet motions is observable. For this reason the modes dominated by the rivulet motion will not be controlled. On the other hand the rivulet motions are driven by the cable acceleration. Hence these will be damped simultaneous with the dominant cable mode.

The open loop state vector equation of motion is given by (4.68) in which the dependence of $\mathbf{A}, \mathbf{b}_0$ and $\mathbf{b}$ on the state vector $\mathbf{z}(t)$ stems from the nonlinear damping term and the time varying tangential acceleration in the rivulet equations of motion. In the following pole placement control design, an equivalent linear rivulet equation is introduced, corresponding to replacing $\zeta_r|\dot{\theta}|^{a_r}$ with an equivalent damping ratio $\zeta_{r,e}$ in (4.53). The linearization of the rivulet damping term is presented in section 4.2.3. Additionally, only the first term in the linearized expression of $\boldsymbol{M}(\boldsymbol{\theta}_S)$ in (4.55) is included. Hereby, $\mathbf{A}$ is assumed a constant matrix in what follows.

At first damped eigenvibrations of (4.68) are considered, corresponding to

$$\dot{\mathbf{z}}(t) = \mathbf{A}\mathbf{z}(t) \tag{4.99}$$

The solution of (4.99) is given as

$$\mathbf{z}(t) = \boldsymbol{\Phi}_j e^{\lambda_j t} \quad , \quad j = 1,\ldots,2N \tag{4.100}$$

where $(\lambda_j, \boldsymbol{\Phi}_j)$ indicates the eigenvalues and eigenvectors of the following linear so-called open loop eigenvalue problem

$$\mathbf{A}\boldsymbol{\Phi}_j = \lambda_j \boldsymbol{\Phi}_j \quad , \quad j = 1,\ldots,2N \tag{4.101}$$

If $(\lambda_j, \boldsymbol{\Phi}_j)$ is an eigensolution to (4.101), so is the complex conjugate $(\lambda_j^*, \boldsymbol{\Phi}_j^*)$. Generally, the eigenvalues are complex and may be written on the form

$$\lambda_j = -\mu_j + i\nu_j \tag{4.102}$$

μ_j specifies the damping of the j^{th} mode, which for a stable mode is less than zero. ν_j indicates the damped angular eigenfrequency of the j^{th} mode. (4.102) may be rewritten on the form

$$\lambda_j = \omega_j\left(-\zeta_j + i\sqrt{1-\zeta_j^2}\right) \tag{4.103}$$

where

$$\omega_j = \sqrt{\mu_j^2 + \nu_j^2} = \left|\lambda_j\right| \tag{4.104}$$

$$\zeta_j = \frac{\mu_j}{\sqrt{\mu_j^2 + \nu_j^2}} \tag{4.105}$$

ω_j and ζ_j may be interpreted as the undamped angular eigenfrequency and the modal damping ratio of the j^{th} mode, respectively. A system is known to be unstable if one of the open loop poles have positive real part, corresponding to $\zeta_j < 0$.

The idea of linear state feedback control is to ensure that the closed loop poles are placed as far to the left in the complex plane as possible. However, an undercritically damped system should be obtained. The pole placement method produces the mentioned control gains. The following single input control is based on, (Porter, et al., 1972). It should be noted that the pole placement method also exist in other forms, (Juang, et al., 2001).

The equivalent damping ratio of the rivulet equations of motion $\zeta_{r,e}$ is at least two order of magnitudes larger than the damping ratio of the cable modes. Then, the $2n$ eigenmodes dominated by the rivulet motions are identified by damping ratios ζ_j as given by (4.105) which are of the order of magnitude as $\zeta_{r,e}$. The corresponding eigenmodes are specified by the index $j = 2m+1, \ldots, 2N$. These modes will not be controlled. The remaining $2m$ modes indicates the modes dominated by cable vibrations. These will be ordered pairwise in ascending order of ν_j corresponding to

$$0 < \nu_1 < \ldots < \nu_m \tag{4.106}$$

The $2N$ eigenvalueproblems defined by (4.101) may be assembled in the following matrix formulation

$$\mathbf{A}\boldsymbol{\Phi} = \boldsymbol{\Phi}\boldsymbol{\Lambda} \tag{4.107}$$

where the modal matrix $\boldsymbol{\Phi}$ and the diagonal eigenvalue matrix $\boldsymbol{\Lambda}$ has the structure

$$\begin{aligned}\boldsymbol{\Phi} &= \left[\boldsymbol{\Phi}_1, \boldsymbol{\Phi}_2, \boldsymbol{\Phi}_3, \cdots \boldsymbol{\Phi}_{2N-1}, \boldsymbol{\Phi}_{2N}\right] \\ &= \left[\boldsymbol{\Phi}_1, \boldsymbol{\Phi}_1^*, \boldsymbol{\Phi}_3, \boldsymbol{\Phi}_3^*, \cdots \boldsymbol{\Phi}_{2N-1}, \boldsymbol{\Phi}_{2N-1}^*\right]\end{aligned} \tag{4.108}$$

$$\boldsymbol{\Lambda} = \begin{bmatrix} \lambda_1 & 0 & \cdots & & 0 \\ 0 & \lambda_2 & \ddots & & \vdots \\ \vdots & \ddots & \ddots & & \\ & & & \lambda_{2N-1} & 0 \\ 0 & \cdots & & 0 & \lambda_{2N} \end{bmatrix} = \begin{bmatrix} \lambda_1 & 0 & \cdots & & 0 \\ 0 & \lambda_1^* & \ddots & & \vdots \\ \vdots & \ddots & \ddots & & \\ & & & \lambda_{2N-1} & 0 \\ 0 & \cdots & & 0 & \lambda_{2N-1}^* \end{bmatrix}$$

The adjoint eigenvalue problem reads

$$\mathbf{A}^T\boldsymbol{\Psi}_j = \lambda_j\boldsymbol{\Psi}_j \quad , \qquad j = 1, \ldots, 2N \tag{4.109}$$

As seen, the eigenvalues of the original and the adjoint eigenvalue problems are identical. Moreover, the corresponding eigenvectors fulfil the orthogonality conditions, (Nielsen, 2004)

$$\boldsymbol{\Psi}_j^T\boldsymbol{\Phi}_k = \begin{cases} 0 & , \quad j \neq k \\ 1 & , \quad j = k \end{cases} \tag{4.110}$$

$$\boldsymbol{\Psi}_j^T\mathbf{A}\boldsymbol{\Phi}_k = \begin{cases} 0 & , \quad j \neq k \\ \lambda_j & , \quad j = k \end{cases} \tag{4.111}$$

Notice that (4.110) and (4.111) presume a proper normalization of either $\boldsymbol{\Psi}$ or $\boldsymbol{\Phi}$ so the scalar product $\boldsymbol{\Psi}_j^T\boldsymbol{\Phi}_j = 1$. Correspondingly, the orthogonality relations may be written in the matrix form

$$\begin{aligned}\boldsymbol{\Psi}^T\boldsymbol{\Phi}&=\mathbf{I}\\ \boldsymbol{\Psi}^T\mathbf{A}\boldsymbol{\Phi}&=\boldsymbol{\Lambda}\end{aligned} \tag{4.112}$$

From (4.111) follows that the original and the adjoint eigenvectors are related as

$$\boldsymbol{\Psi}=\left(\boldsymbol{\Phi}^{-1}\right)^T \tag{4.113}$$

(4.109) may be assembled on the matrix form

$$\begin{aligned}\mathbf{A}^T\boldsymbol{\Psi}&=\boldsymbol{\Psi}\boldsymbol{\Lambda}\\ \boldsymbol{\Psi}&=\left[\boldsymbol{\Psi}_1\boldsymbol{\Psi}_1^*\boldsymbol{\Psi}_2\boldsymbol{\Psi}_2^*\cdots\boldsymbol{\Psi}_N\boldsymbol{\Psi}_N^*\right]\end{aligned} \tag{4.114}$$

The order of the eigenvectors of $\boldsymbol{\Psi}$ follow the same rule as those of $\boldsymbol{\Phi}$.

The lowest $2N_1 < 2m$ modes (the $2N_1$ modes with lowest damped eigenfrequency ν_j) will be controlled. In this respect the gain vector $\mathbf{g}_{PP}$ is chosen as a linear combination of the lowest $2N_1$ modes of the adjoint eigenvectors

$$\mathbf{g}_{PP}=\sum_{j=1}^{2N_1} g_j\boldsymbol{\Psi}_j \tag{4.115}$$

where g_j denotes the modal control gains which will fulfil $g_{2k}=g_{2k-1}^*$ for $k=1,\ldots,N_1$. Insertion of (4.115) in (4.98) provides the following closed loop system matrix

$$\overline{\mathbf{A}}=\mathbf{A}-\mathbf{b}\sum_{l=1}^{2N_1} g_l\boldsymbol{\Psi}_l^T \tag{4.116}$$

The eigenvalues ρ_j and eigenmodes $\bar{\boldsymbol{\Phi}}_j$ of $\overline{\mathbf{A}}$ are denoted the closed loop eigenvalues and eigenmodes. These fulfil

$$\overline{\mathbf{A}}\bar{\boldsymbol{\Phi}}_j=\rho_j\bar{\boldsymbol{\Phi}}_j \quad , \quad j=1,\ldots,2N \tag{4.117}$$

Again, the closed loop eigenmodes are ordered after the same principle as the open loop eigenmodes. It follows from (4.110) and (4.116) that

$$\overline{\mathbf{A}}\boldsymbol{\Phi}_k=\mathbf{A}\boldsymbol{\Phi}_k=\lambda_k\boldsymbol{\Phi}_k \quad , \quad k=2N_1+1,\ldots 2N \tag{4.118}$$

This means that $\rho_k=\lambda_k$ and $\bar{\boldsymbol{\Phi}}_k=\boldsymbol{\Phi}_k$ for $k=2N_1+1,\ldots,2N$. Hence, the eigenvalues and eigenvectors of the uncontrolled modes of the closed loop system are identical to those of the open loop system.

Because the open loop eigenvectors $\boldsymbol{\Phi}_j$, $j=1,\ldots,2N$ are linearly independent, the closed loop eigenvectors can be expanded in the vector base formed by the open loop eigenvectors

$$\bar{\boldsymbol{\Phi}}_j=\sum_{k=1}^{2N} d_{jk}\boldsymbol{\Phi}_k \quad , \quad j=1,\ldots,2N_1 \tag{4.119}$$

Insertion of (4.119) and (4.116) in (4.117) for $j=1,\ldots,2N_1$ and use the orthogonality property (4.110) provides

$$\begin{aligned}&\left(\mathbf{A}-\mathbf{b}\sum_{l=1}^{2N_1} g_l\boldsymbol{\Psi}_l^T\right)\sum_{k=1}^{2N} d_{jk}\boldsymbol{\Phi}_k=\rho_j\sum_{k=1}^{2N} d_{jk}\boldsymbol{\Phi}_k\\ &\Downarrow \qquad\qquad , \quad j=1,\ldots,2N\\ &\sum_{k=1}^{2N} d_{jk}\lambda_k\boldsymbol{\Phi}_k-\mathbf{b}\sum_{l=1}^{2N_1} d_{jl}g_l=\sum_{k=1}^{2N} d_{jk}\rho_j\boldsymbol{\Phi}_k\end{aligned} \tag{4.120}$$

Further, the vector $\mathbf{b}$ may be decomposed in the vector base formed by the open loop eigenvectors

$$\mathbf{b} = \sum_{k=1}^{2N} b_k \boldsymbol{\Phi}_k \tag{4.121}$$

where

$$b_k = \boldsymbol{\Psi}_k^T \mathbf{b} \quad , \quad k = 1,\ldots,2N \tag{4.122}$$

Insertion of (4.121) in (4.120) provides the following vector identities

$$\sum_{k=1}^{2N} \left(\rho_j - \lambda_k\right) d_{jk} \boldsymbol{\Phi}_k + \sum_{k=1}^{2N} \left(b_k \sum_{l=1}^{2N_1} d_{jl} g_l \right) \boldsymbol{\Phi}_k = 0 \quad , \quad j = 1,\ldots,2N_1 \tag{4.123}$$

(4.123) is equivalent to the following $2N_1 \times 2N$ linear equations

$$\left(\rho_j - \lambda_k\right) d_{jk} + b_k \sum_{l=1}^{2N_1} d_{jl} g_l = 0 \quad , \quad j = 1,\ldots,2N_1 \quad , \quad k = 1,\ldots,2N \tag{4.124}$$

For fixed j, (4.124) represents a system of homogenous linear equations for the determination of d_{jk}, $k = 1, \ldots, 2N$. On matrix form these equations read

$$\begin{bmatrix} \rho_j - \lambda_1 + b_1 g_1 & b_1 g_2 & \cdots & b_1 g_{2N_1} & 0 & \cdots & 0 \\ b_2 g_1 & \rho_j - \lambda_2 + b_2 g_2 & \cdots & b_2 g_{2N_1} & 0 & \cdots & 0 \\ \vdots & \vdots & \ddots & \vdots & \vdots & \ddots & \vdots \\ b_{2N_1} g_1 & b_{2N_1} g_2 & \cdots & \rho_j - \lambda_{2N_1} + b_{2N_1} g_{2N_1} & 0 & & 0 \\ b_{2N_1+1} g_1 & b_{2N_1+1} g_2 & \cdots & b_{2N_1+1} g_{2N_1} & \rho_j - \lambda_{2N_1+1} & 0 & 0 \\ \vdots & \vdots & & \vdots & \vdots & \ddots & \vdots \\ b_{2N} g_1 & b_{2N} g_2 & \cdots & b_{2N} g_{2N_1} & 0 & \cdots & \rho_j - \lambda_{2N} \end{bmatrix} \begin{bmatrix} d_{j\,1} \\ d_{j\,2} \\ \vdots \\ d_{j\,2N_1} \\ d_{j\,2N_1+1} \\ \vdots \\ d_{j\,2N} \end{bmatrix} = \begin{bmatrix} 0 \\ 0 \\ \vdots \\ 0 \\ 0 \\ \vdots \\ 0 \end{bmatrix} \tag{4.125}$$

Non-trivial solutions for d_{jl} where $l = 1, \ldots, 2N_1$ requires that the coefficient matrix of the first $2N_1$ equations are singular. Assume that these solutions are given as

$$d_{jk} = \frac{b_k}{\rho_j - \lambda_k} \quad , \quad k = 1,\ldots,2N_1 \tag{4.126}$$

Then, the first $2N_1$ equations of (4.125) may be written as

$$\begin{aligned} d_{j1} + d_{j1}\left(d_{j1} g_1 + d_{j2} g_2 + \ldots + d_{j2N_1} g_{2N_1}\right) &= 0 \\ d_{j2} + d_{j2}\left(d_{j1} g_1 + d_{j2} g_2 + \ldots + d_{j2N_1} g_{2N_1}\right) &= 0 \\ &\vdots \\ d_{j2N_1} + d_{j2N_1}\left(d_{j1} g_1 + d_{j2} g_2 + \ldots + d_{j2N_1} g_{2N_1}\right) &= 0 \end{aligned} \tag{4.127}$$

Hence, (4.126) is indeed a solution to (4.125) for arbitrary j if

$$d_{j1} g_1 + d_{j2} g_2 + \ldots + d_{j2N_1} g_{2N_1} = -1 \tag{4.128}$$

Then, the solution (4.126) also applies for the remaining equations, i.e.

$$d_{jk} = \frac{b_k}{\rho_j - \lambda_k} \quad , \quad k = 2N_1 + 1,\ldots,2N \tag{4.129}$$

It can be shown that the coefficient matrix of (4.125) has the rank $2N_1 - 1$. This means that save for an arbitrary common factor the solution (4.126) is unique if (4.128) is fulfilled.

The idea of the pole placement method is to prescribe the eigenvalues ρ_j, $j = 1, \ldots, 2N_1$. Hence, d_{jk}, $k = 1, \ldots, 2N_1$ in (4.126) are known (i.e. prescribed quantities for arbitrary indices j). Then, the unknown gains $g_1, g_2, \ldots, g_{2N_1}$ can be determined by formulating (4.128) for $j = 1, \ldots, 2N_1$. This results in the linear equations

$$\begin{bmatrix} \frac{b_1}{\rho_1-\lambda_1} & \frac{b_2}{\rho_1-\lambda_2} & \cdots & \frac{b_{2N_1}}{\rho_1-\lambda_{2N_1}} \\ \frac{b_1}{\rho_2-\lambda_1} & \frac{b_2}{\rho_2-\lambda_2} & \cdots & \frac{b_{2N_1}}{\rho_2-\lambda_{2N_1}} \\ \vdots & \vdots & \ddots & \vdots \\ \frac{b_1}{\rho_{2N_1}-\lambda_1} & \frac{b_2}{\rho_{2N_1}-\lambda_2} & \cdots & \frac{b_{2N_1}}{\rho_{2N_1}-\lambda_{2N_1}} \end{bmatrix} \begin{bmatrix} g_1 \\ g_2 \\ \vdots \\ g_{2N_1} \end{bmatrix} = \begin{bmatrix} -1 \\ -1 \\ \vdots \\ -1 \end{bmatrix} \tag{4.130}$$

The solution of (4.130) can be shown to be

$$g_j = -\frac{1}{b_j} \frac{\prod_{k=1}^{2N_1} (\rho_k - \lambda_j)}{\prod_{\substack{k=1 \\ k \neq j}}^{2N_1} (\lambda_k - \lambda_j)} \quad , \quad j = 1, \ldots, 2N_1 \tag{4.131}$$

In the present case the closed loop eigenvalues ρ_j will be chosen so the undamped eigenfrequencies ω_j are equal to those of the open loop system, c.f. (4.103). Only the closed loop damping ratios $\bar{\zeta}_j$ are chosen. Hence, ρ_j is given as

$$\rho_j = \omega_j \left(-\bar{\zeta}_j \pm i \sqrt{1 - \bar{\zeta}_j^2} \right) \quad , \quad j = 1, \ldots, 2N_1 \tag{4.132}$$

4.3.4 Active control by combined pole placement and integral control

In addition to the active controller, an integral controller is added to the system. The part of the control force from integral control is expected to increase the damping ratio of low frequency modes.

Especially, the integral control will eliminate any static response of the cable. In the current case of rain/wind induced vibrations such an offset is present due to the static load from the considered mean wind. The integral control force is given as

$$u(t) = \gamma_{IC} \int_{-\infty}^{t} v_d(\tau) d\tau \quad , \qquad \gamma_{IC} > 0 \tag{4.133}$$

where γ_{IC} is the integral control gain which must be determined by numerical trials. From (4.73) and (4.74) follows

$$u(t) = \gamma_{IC} \mathbf{n}^T \mathbf{A}_i \int_{-\infty}^{t} \mathbf{v}_S(\tau) d\tau = \boldsymbol{\gamma}_{IC}^T \int_{-\infty}^{t} \mathbf{w}(\tau) d\tau \tag{4.134}$$

where the gain vector $\boldsymbol{\gamma}_{\mathrm{IC}}$ of dimension $N \times 1$ is given as

$$\boldsymbol{\gamma}_{IC} = \begin{bmatrix} \gamma_{IC} \mathbf{A}_i^T \mathbf{n} \\ \mathbf{0}^T \end{bmatrix} \tag{4.135}$$

Expressed by the state vector $\mathbf{z}(t)$, (4.134) allows the form

$$u(t) = \mathbf{g}_{IC}^T \int_{-\infty}^{t} \mathbf{z}(\tau) d\tau \tag{4.136}$$

where the integral gain vector $\mathbf{g}_{\mathrm{IC}}$ of dimension $2N \times 1$ is given as

$$\mathbf{g}_{IC} = \begin{bmatrix} \boldsymbol{\gamma}_{IC} \\ \mathbf{0} \end{bmatrix} \tag{4.137}$$

If the indicated components are specified to non-zero values, it means that a stiffness contribution is introduced in the control force, which has already been accounted for by the pole placement term.

Insertion of (4.96) and (4.136) in (4.78) the systems equation of motion provides the following closed loop state equation

$$\dot{\mathbf{z}}(t) = \overline{\mathbf{A}}\mathbf{z}(t) - \mathbf{b}_0 + b_1 \int_{-\infty}^{t} \mathbf{z}(\tau) d\tau \tag{4.138}$$

where

$$\overline{\mathbf{A}} = \mathbf{A} - \mathbf{b}\mathbf{g}_{PP}^{T} \tag{4.139}$$

$$b_1 = \mathbf{b}\mathbf{g}_{IC}^{T} \tag{4.140}$$

where $b_1 = b_1(\boldsymbol{\theta}_S)$.

4.3.5 Active control of axial forces

This approach operates by control of the elongation of the cable ΔL through an actuator at one of the support points. Hereby, a variation in the tension F_0 is generated through the cable. By applying a control law for these elongations, the vibrations of the cable may be damped. First a 2DOF system in modal coordinates is accounted for, after which two different control laws are described. The following is supported by figure 22, where the cable is illustrated in the equilibrium state with initial sag f and chord length L. The in-plane displacements are denoted v and the out-of-plane displacements are denoted w.

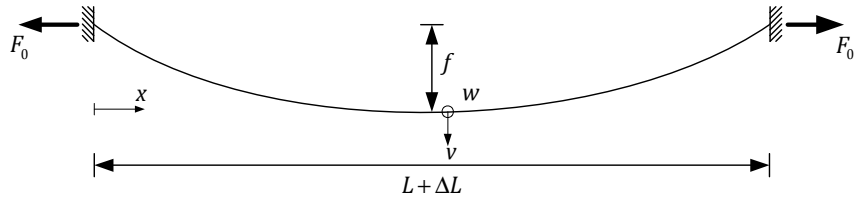

Figure 22: Cable in the equilibrium state.

Only the fundamental in-plane and out-of-plane modes are considered. In the shallow cable case, the eigenfrequencies will be pair wise closely spaced. As the static equilibrium plane works as a symmetry plane the eigenvibrations decouple in the in-plane mode which only affects $v(x,t)$ and the out-of-plane mode which only affects $w(x,t)$. The modal expansion for the displacements v and w becomes

$$\begin{aligned} w(x,t) &\simeq \Phi_1(x) q_1(t) \\ v(x,t) &\simeq \Phi_2(x) q_2(t) \end{aligned} \tag{4.141}$$

where $\Phi_1(x)$ and $\Phi_2(x)$ are the two lowest out-of-plane and in-plane eigenmodes and $q_1(t)$ and $q_2(t)$ are the related modal coordinates. Retaining geometrical nonlinearities up to cubic order, the following coupled ordinary differential equations of motion for modal coordinates $q_1 = q_1(t)$ and $q_2 = q_2(t)$ has been derived as follows, (Larsen, 2005)

$$\begin{aligned} &\ddot{q}_1 + 2\zeta_1\omega_1\dot{q}_1 + \omega_1^2\left(1+e(t)\right)q_1 + \beta_1 q_1 q_2 + q_1\left(\gamma_1 q_1^2 + \gamma_2 q_2^2\right) = 0 \\ &\ddot{q}_2 + 2\zeta_2\omega_2\dot{q}_2 + \omega_2^2\left(1+\alpha e(t)\right)q_2 + \beta_2 q_1^2 + \beta_3 q_2^2 + q_2\left(\gamma_3 q_1^2 + \gamma_4 q_2^2\right) = -\delta e(t) \end{aligned} \tag{4.142}$$

Where ω_1 and ω_2 are the fundamental angular eigenfrequencies and ζ_1, ζ_2 are the corresponding modal damping ratios, respectively. Furthermore α, β_1, β_2, β_3, β_4, γ_1, γ_2, γ_3, γ_4, and δ are parameters, which depends on the eigenmodes $\Phi_1(x)$, $\Phi_2(x)$ in addition to the sag f, the fundamental angular eigenfrequency ω_0 of a taut wire, and the Irvine parameter given as follows

$$\gamma^2 = 64\frac{EA}{F_0}\frac{f^2}{L_0} \tag{4.143}$$

where L_0 denotes the length of the parabolic suspension. In (4.142) the non-dimensional representation of the chord elongation is of the order of magnitude 1 and defined as

$$e(t) = \frac{EA}{F_0}\frac{\Delta L(t)}{L} \tag{4.144}$$

As seen from (4.142) the chord elongation both implies a parametric excitation of both modal coordinates and an additive load term on the in-plane mode.

Axial vibration control implies the specification of a control law via the axial elongation $e(t)$. Basically two approaches are possible, in which the control is performed via the additive and the parametric load terms, respectively. The two approaches are consequently described.

Control of the additive load

Axial control via the additive load implies the following feedback control, (Fujino, et al., 1993)

$$e(t) = c\dot{q}_2 \quad , \quad c > 0 \tag{4.145}$$

Then, by insertion of (4.145) in (4.142) the closed loop system becomes

$$\begin{aligned}
&\ddot{q}_1 + 2\zeta_1\omega_1\dot{q}_1 + \omega_1^2(1 + c\dot{q}_2)q_1 + \beta_1 q_1 q_2 + q_1\left(\gamma_1 q_1^2 + \gamma_2 q_2^2\right) = 0 \\
&\ddot{q}_2 + \left(2\zeta_2\omega_2 + \delta c\right)\dot{q}_2 + \omega_2^2(1 + \alpha c\dot{q}_2)q_2 + \beta_2 q_1^2 + \beta_3 q_2^2 + q_2\left(\gamma_3 q_1^2 + \gamma_4 q_2^2\right) = 0
\end{aligned} \tag{4.146}$$

As seen the control law increases the damping of the in-plane mode. Moreover, in harmonic motions

$$\int_0^{T_2} \dot{q}_2(t)q_2(t)dt = 0 \tag{4.147}$$

Hence, the control law is not supposed to have significant influence on the stiffness of the controlled fundamental in-plane mode.

Control of parametric excitation

Axial control via the parametric load term implies the following feedback control, (Wang, et al., 2007)

$$e(t) = c\frac{\dot{q}_2}{q_2} \quad , \quad c > 0 \tag{4.148}$$

Then, by insertion of (4.148) in (4.142) the closed loop system becomes

$$\begin{aligned}
&\ddot{q}_1 + 2\zeta_1\omega_1\dot{q}_1 + \omega_1^2\left(1 + c\frac{\dot{q}_2}{q_2}\right)q_1 + \beta_1 q_1 q_2 + q_1\left(\gamma_1 q_1^2 + \gamma_2 q_2^2\right) = 0 \\
&\ddot{q}_2 + \left(2\zeta_2\omega_2 + \frac{\delta c}{q_2} + \alpha c\dot{q}_2\right)\dot{q}_2 + \omega_2^2 q_2 + \beta_2 q_1^2 + \beta_3 q_2^2 + q_2\left(\gamma_3 q_1^2 + \gamma_4 q_2^2\right) = 0
\end{aligned} \tag{4.149}$$

The latter control law is problematic because $e(t)$ may be very large, whenever $q_2 = 0$.

Generally the control of axial forces requires very large actuators. Since the coordinates are measured by sensors along the cable, the control is not collocated. Hence, significant observation- or control spillover effects may be present. For these reasons, this type of control will not be considered any further.

5 Simulation

The numerical model introduced in chapter 4 is used to simulate rain/wind induced loadings on a stay-cable at a cable stayed bridge. The results of repeated simulations from different damping configurations will be presented and compared in the following.

A cable with chord length $L = 150m$, radius $R = 0.07m$, axial stiffness $AE = 2.17 \cdot 10^8 N$, mass per unit length $\mu = 108kg/m$, and a prestressing force of $F_0 = 1.1 \cdot 10^6 N$ is considered in the global XY-plane. The cable chord has the initial angle of inclination $\varphi_0 = 30°$. The four lowest undamped in-plane angular eigenfrequencies become

$$\omega_1 = 2.52s^{-1}\ ,\ \omega_2 = 4.70s^{-1}\ ,\ \omega_3 = 7.13s^{-1}\ ,\ \omega_4 = 9.63s^{-1} \tag{5.1}$$

In the simulations a mean wind U_0 is applied which has a wind yaw angle $\beta = 35°$. The damper will be placed with a distance $a = 3m$ between the lower support point and the connection point between the damper and the cable and the damper has an angle of inclination $\Psi = 60°$ with the global X-axis. By choosing $a = 3m$ the connection is $1.5m$ above the bridge deck level which will ease possible maintenance tasks. Furthermore, according to (4.83) the modal damping ratio becomes $\zeta_{opt} = \zeta_1 = 0.01$, for a linear viscous damper tuned to the first mode of vibration. The above is illustrated in figure 23.

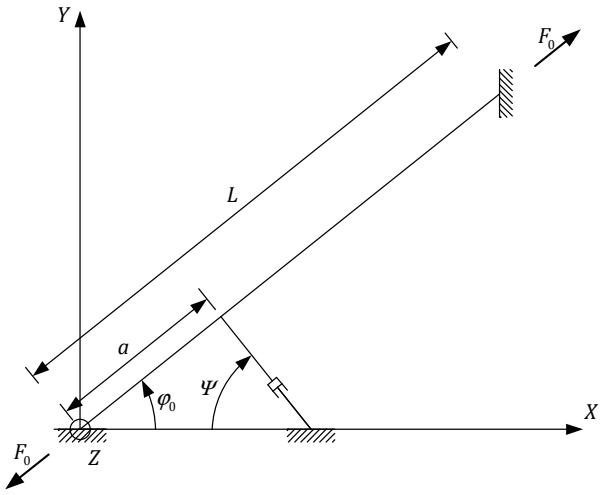

Figure 23: Definition of general parameters in the numerical model.

In what follows the efficiency of the considered damping strategies will be evaluated partly on a comparison of the mid-point displacements of the cable, and partly on the mean damper power estimated from

$$P_d = \frac{1}{T}\int_0^T u(\tau)\dot{v}_d(\tau)d\tau \tag{5.2}$$

The damping strategies are handled by separate colours when the results are displayed. The following damper configurations are considered

1. Rain/wind induced vibrations without control **[black]**
2. Vibration control by passive viscous damping **[blue]**
3. Vibration control by semi-active MR-damping **[green]**
4. Active vibration control by pole placement **[red]**
5. Active vibration control by combined pole placement and integral control **[purple]**

5.1 Rain/wind induced vibrations without control

The obtained results depend on the spatial discretization as measured by the number n of finite elements. In figure 24, the results of the mid-point cable displacements, for repeated simulations subjecting the system to a mean wind speed $U_0 = 11.5m/s$ during $15s$ with different cable discretizations, are displayed. The vibration amplitude obtained for 15 elements converge satisfactory for which $n = 15$ is used in the following.

In order to achieve the distance requirement $a = 3m$ to the connection point of the damper, an additional node is added at the distance a from the lower support point along the cable chord. The remaining cable length above the support point of the damper is subdivided in $(n-1)$ equal elements.

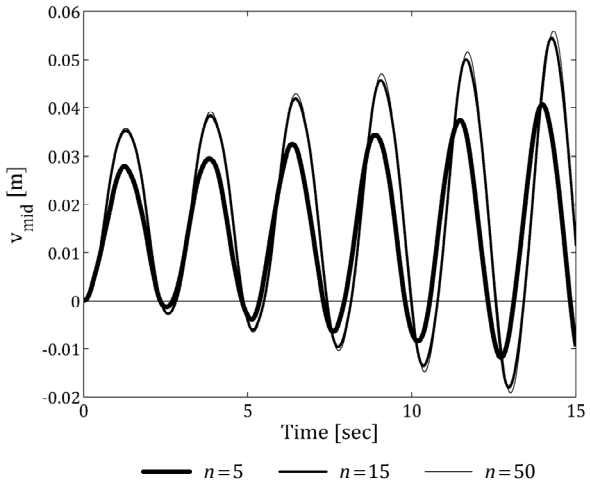

Figure 24: Vibration amplitude as a function of number of elements.

As mentioned in chapter 2 the equilibrium position θ_0 of the upper rivulet depends on the mean wind velocity. The response of the system, when U_0 is varied within the considered wind range $9m/s \leq U_0 \leq 15m/s$, is clarified by repeated simulations. The results of maximum cable displacements and rivulet oscillations are displayed in figure 25 when sample times of $100s$ are considered.

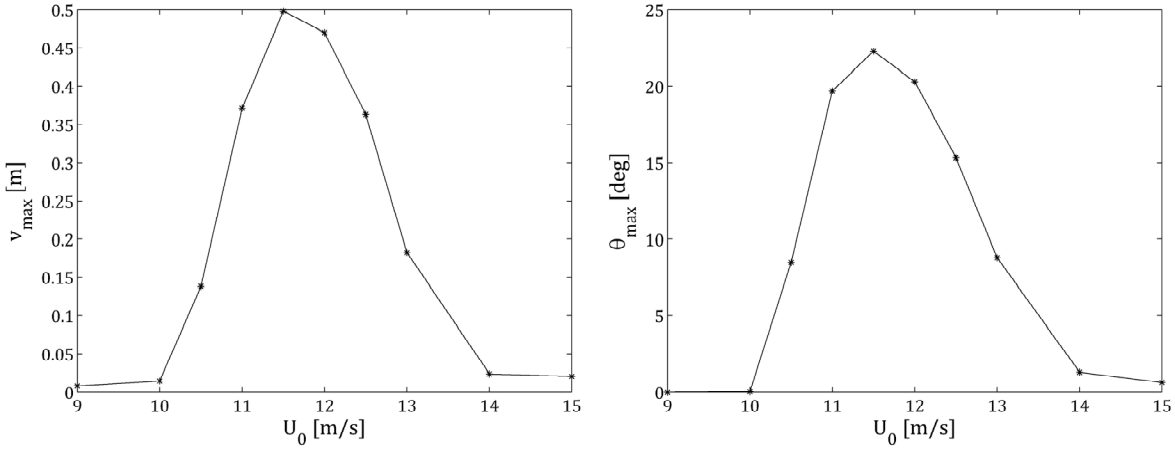

Figure 25: Maximum cable displacements and rivulet oscillation amplitudes.

The ranges $U_0 < 10.5m/s$ and $U_0 > 13m/s$ are combined and denoted the outer range. Here, the cable displacement and the rivulet oscillations are kept at a very low level. In the range of approximately $10.5m/s \leq U_0 \leq 13m/s$ aerodynamic instability occur which leads to large cable displacements and rivulet oscillations. Hence, the rain/wind induced vibrations are indeed dependent on the mean wind velocity.

By considering the variation of the aerodynamic coefficients c.f. figure 11, the dependence of the mean wind velocity on the static position of the rivulet c.f. figure 14, and the definition of the effective wind angle of attack (4.13), the critical interval of the effective wind angle of attack is found to be $56° \leq \alpha_{eff} \leq 72°$. As seen in figure 11, $\partial \bar{c}_L / \partial \alpha$ is negative in the critical interval of α_{eff} where aeroelastic instability occurs. It is well known that negative values of the gradient of the lift coefficient are crucial for triggering galloping instability, (Den Hartog, 1956). When U_0 is in the outer range, α_{eff} will move out of the indicated critical interval because the static position of the rivulet $\theta_0(U_0)$ is changed. As maximum displacement amplitudes are observed for $U_0 = 11.5m/s$ this mean wind velocity is used in all the simulations.

Related to the above it is found that the cable displacement and rivulet oscillations stabilize when U_0 is in the outer range. On the contrary, the displacement amplitude increase rapidly in the range where aerodynamic instability occur which is also the reason for the high amplitude oscillations of the rivulet. In general a static offset of the cable displacement exists due to the mean wind and the related load p_0, c.f. (4.52). The maximum cable displacement response and rivulet oscillation response are found at the mid-point and on an element at mid-point position, respectively. The indicated responses are displayed in figure 26.

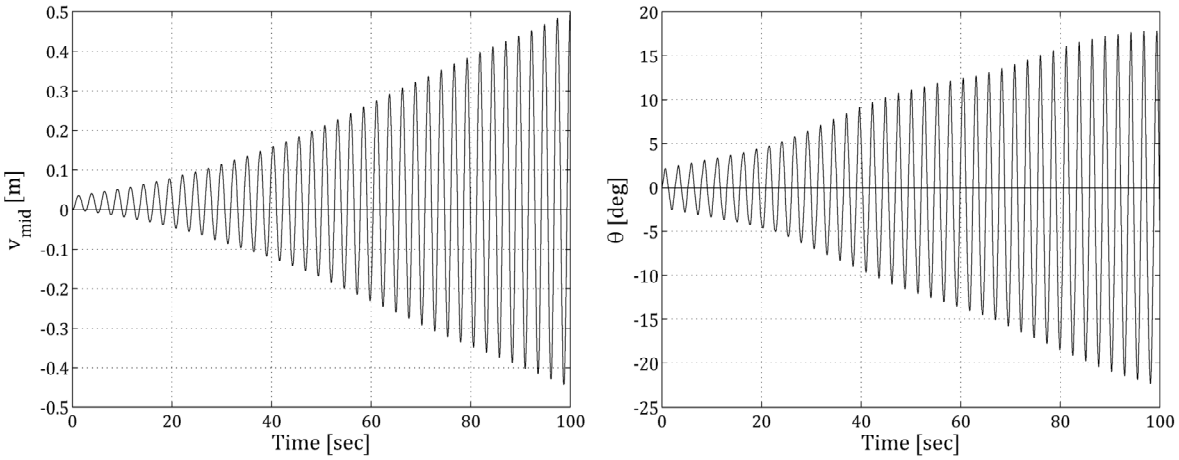

Figure 26: Maximum displacement response of the cable and rivulet oscillations in the uncontrolled case.

Results from wind tunnel tests and field observations indicate that the cable- and rivulet displacement amplitudes reach a stationary peak-to-peak value, (Hikami, et al., 1988). The self-limitation of the cable vibration is due to geometric non-linear stiffness terms, which are ignored in the present numerical model. Therefore, the results in figure 26 does not rightfully describe the real behaviour of the cable. However, the maximum cable displacement amplitude $v_{mid} = 0.5m$ after $100\ s$ is used in the following as a reference value in order to compare the uncontrolled- and controlled vibrations.

Solving the eigenvalue problem corresponding to the damped eigenvibrations (4.99) leads to determination of the uncontrolled in-plane cable modes of vibration. These are determined as the modes with negative value of the modal damping ratio. When $U_0 = 11.5m/s$ the four unstable modes have modal damping ratios corresponding to

$$\zeta_1 = -0.0085\ ,\ \zeta_2 = -0.0038\ ,\ \zeta_3 = -0.0017\ ,\ \zeta_4 = -0.0004 \tag{5.3}$$

As the load on each finite element is the same, standing waves are found to dominate the vibration response.

5.2 Vibration control by passive viscous damping

According to (4.82) the optimal damping coefficient becomes $c_{opt} \approx 1.64 \cdot 10^5 Ns/m$ when the distance to the damper is $a = 3m$ and the damper is tuned to the first in-plane cable mode of vibration. By doing so, all closed loop poles have negative real part and the modal damping ratios related to the cable are within the range $\bar{\zeta}_j \in]0,1[$. Then, asymptotic stability is expected as the system is considered to be linear.

The maximum displacement response of the cable and the rivulet when controlled by the viscous damper, as displayed in figure 27, are found at the mid-point of the cable. As seen, the vibration amplitude of the cable does not converge towards zero but towards a stationary value of $0.25m$ reached after $280s$. The corresponding rivulet oscillation amplitude is $13°$. The explanation must lie within the linearized approximations as the results do not show the expected behaviour of a linear system.

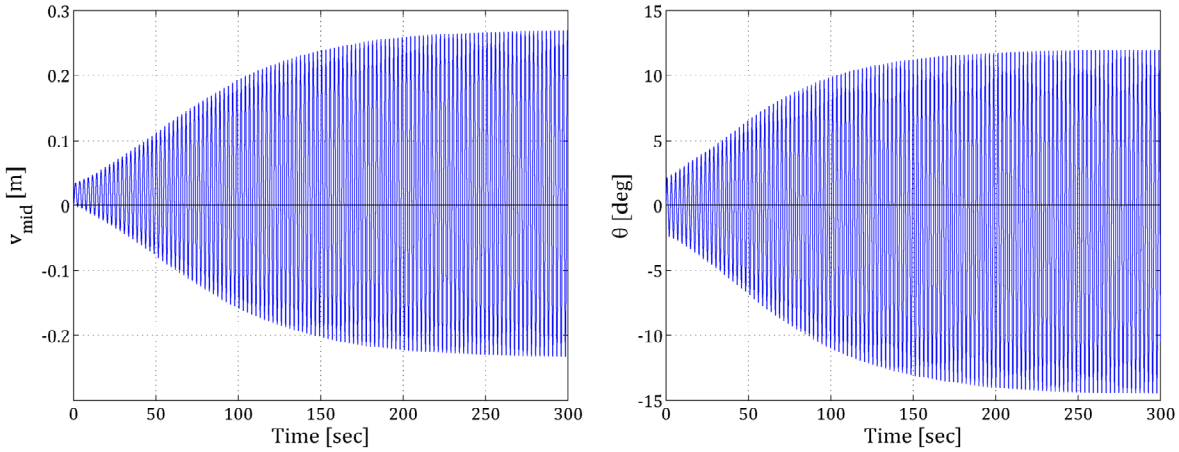

Figure 27: Maximum displacement response of the cable and the rivulet when the vibrations are controlled by passive viscous damping.

The control law for the passive viscous damping, as described in section 4.3.1, depends on $\dot{v}_d(t)$. Because the response is dominated by the first mode, $v_d(t)$ develops in a similar way as $v_{mid}(t)$ in figure 27, which explains the development of the control force as illustrated in figure 28a. In figure 28b the mean damping power performed by the linear viscous damper is displayed. The mean power converges after $1600s$ at $56W$.

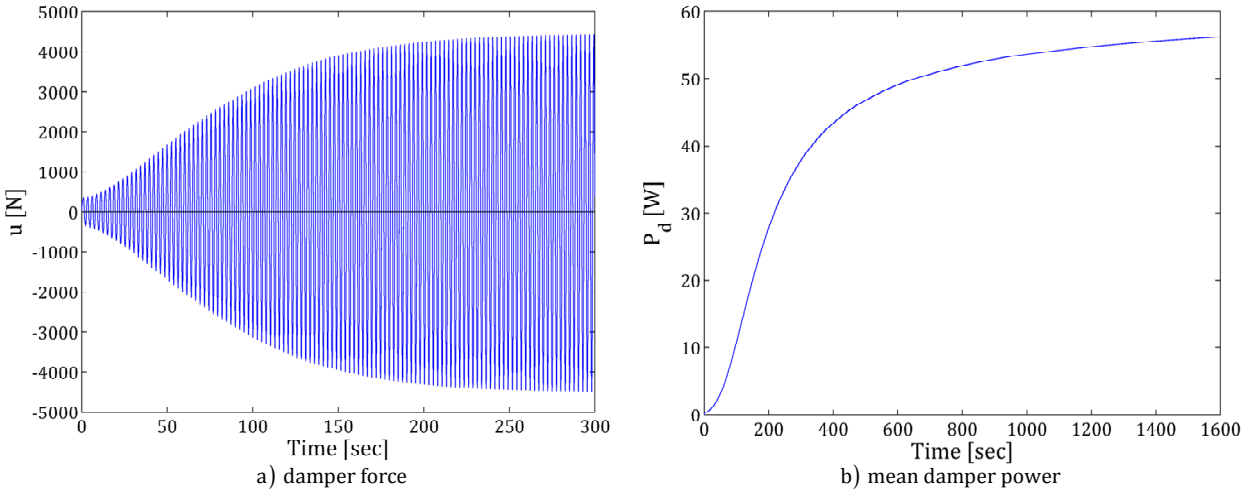

Figure 28: Development of the control force and the damper effect for passive viscous damping.

Compared to the reference value of the uncontrolled system, the passive viscous damper reduce the maximum cable displacement after $100s$ by 35%. It should be noted that in case of reduced values of a/L, the efficiency of the passive viscous damper is reduced.

5.3 Vibration control by semi-active MR-damping

The idea in the semi-active damping strategy is to change the viscosity of the fluid in the damper according to the response of the system and hereby obtain a better performance, relative to the passive viscous damper. As mentioned in section 4.3.2 a number of parameters must be calibrated for optimal

performance of the MR-damper. These should be chosen in such a way that the best possible damping is achieved. Especially, it must be ensured that locking is avoided, since this only implies a shorter chord length of the cable, without any energy dissipation.

The control law for the MR-damper are outlined in section 4.3.2 and the main expressions are repeated below for convenience

$$u(t) = k_0 v_d(t) + c_0 \dot{v}_d(t) + p_f(t) z(t) - p_0 \tag{5.4}$$

$$c_0(t) = c_{0,0} + c_{0,1} y(t) \tag{5.5}$$

$$p_f(t) = p_{f,0} + p_{f,1} y(t) \tag{5.6}$$

In the present case the parameters are calibrated by separately evaluating the effect of each term in the control force (5.4) by keeping the remaining terms at zero values. However, the damping coefficient $c_{0,0}$ corresponding to the optimal damping coefficient of the passive viscous damper is included in all cases. This implies that $c_{0,0} = c_{opt} = 1.64 \cdot 10^5 Ns/m$.

The parameter β_f is chosen in relation to the maximum peak-values of $v_d(t)$ in order to obtain a voltage output within a specified range. One of the largest advantages with the MR-damper is the small use of power for which V_{max} is assumed to be $10V$. The static offset implies higher positive than negative peak-values. Therefore, it is necessary to adjust the peak-values of $v_d(t)$ in order to obtain a regular variation of the voltage input. This may be done by considering half the difference between the considered- and the previous peak value. Furthermore, it is assumed that $p_0 = 0$ and the parameters η and σ are constant as they depend on the damper materials. In the present case $\eta = 200 s^{-1}$ and $\sigma = 5 \cdot 10^4 m^{-1}$, which is chosen according to (Zhou, et al., 2006).

From figure 29a it is realized that the stiffness term will introduce an asymmetric contribution to the control force as the static offset implies greater positive than negative displacement amplitudes. The stiffness term is evaluated by considering the mid-point displacement response of the cable in figure 29b when k_0 is included. Considering other values of k_0 shows the same tendency. It appears that the stiffness term increase the vibration response for which reason it should be disregarded. The physical explanation is that the stiffness term reduces the damper motion $v_d(t)$ somewhat, and hence reduce the energy dissipation. This may as well explain the reduced vibration period.

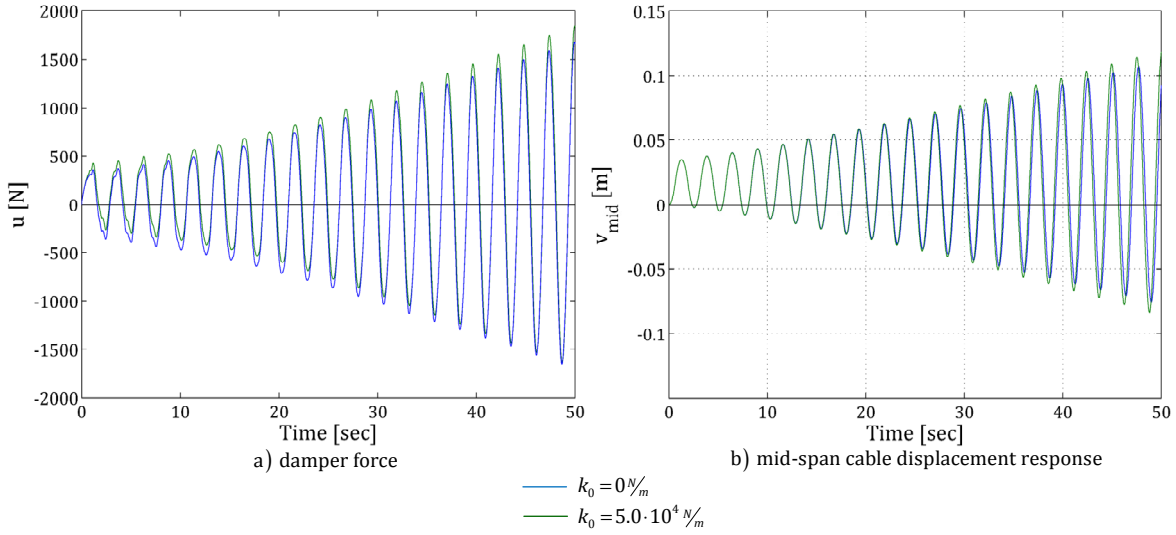

Figure 29: Results when the stiffness term is included.

Since $y(t)$ is non-negative it follows from (5.5) that the time dependent damping coefficient always is larger than the optimal viscous damping coefficient $c_{0,0}$, which suggests a reduced damping effect. As seen in figure 30a the damper force is increased correspondingly to the term $c_{0,1} y(t)$. Due to the reduced

efficiency, the mid-point cable displacement is also increased as seen in figure 30b. These observations suggests that the $c_{0,1}$ coefficient should be disregarded.

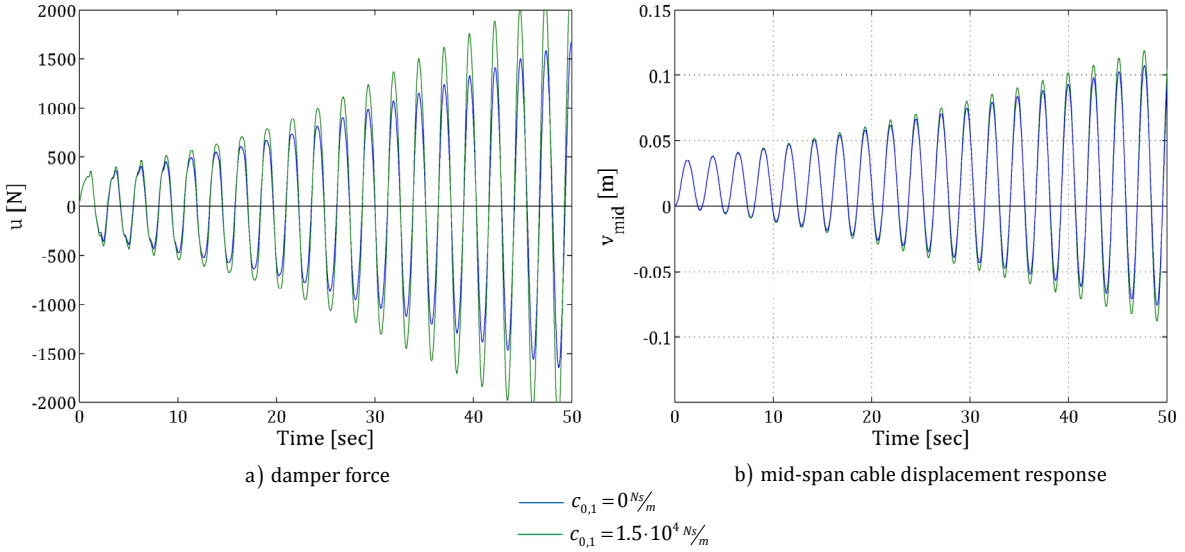

Figure 30: Results when the damping term is varied.

The friction term (5.6) controls both the voltage requirement by (4.93) and contributes to the total control force. When choosing the test values both applications must be taken into consideration. Different approaches exist concerning how the voltage requirement is determined. The parameters can either be chosen in a way so the maximum voltage is reached at small vibrations, in a way so the maximum voltage is reached only for the maximum vibrations of the cable, or somewhere in between. All approaches are considered in the numerical trials.

Due to the non-dimensional hysteretic variable $z(t)$ and the intrinsic variable $y(t)$, the damper force is changed relative to the optimal linear viscous damper force, as seen in figure 31a. The corresponding maximum displacement response of the cable is found at the mid-point as displayed in figure 31b.

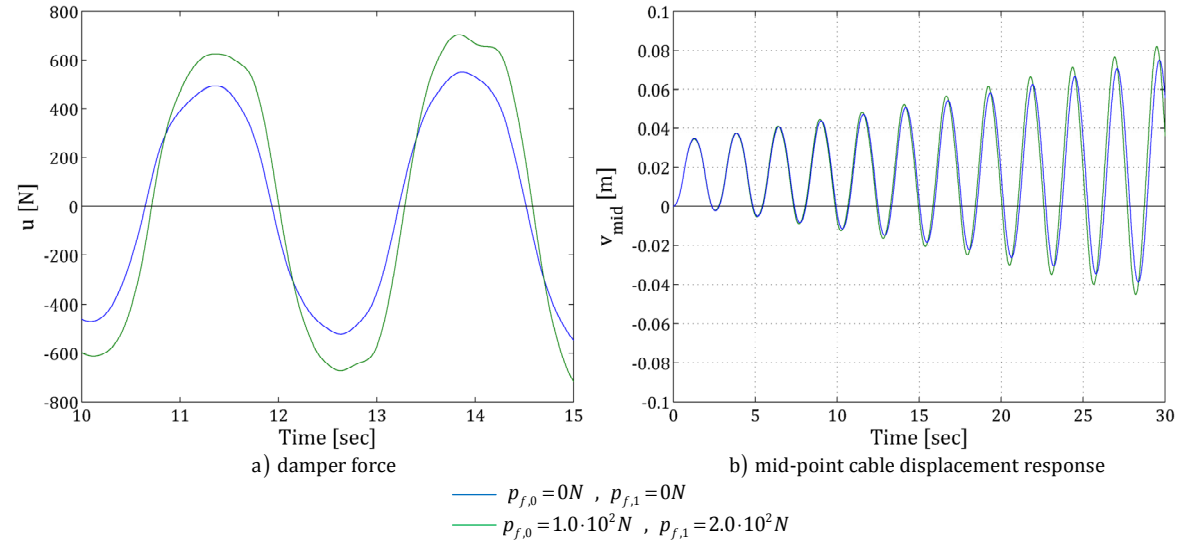

Figure 31: General findings when the friction term is included.

The above indicates that the stationary mean damper power is decreased when the friction term is included. This is in consistence with the results as shown in table 1, where the mean damper power is shown for different configurations of the relationship between $p_{f,0}$ and $p_{f,1}$. The intention is to describe the

results in a general way, but in fact the calibration of the friction term is much more comprehensive due to the interaction between β_f, $p_{f,0}$ and, $p_{f,1}$. Hence, the results in table 1 should be considered with some caution. The results suggest that the friction term should be disregarded.

Table 1: Mean damper effect when the friction terms are varied.

	$p_f = 0$	$p_{f,0} = p_{f,1}$	$p_{f,0} = 0.5p_{f,1}$	$p_{f,0} = 2p_{f,1}$
$P_d[W]$	56	50	51	45

From the results indicated above it must be concluded that the MR-damper in the present case will not be more efficient than the passive viscous damper.

5.4 Active vibration control by pole placement

As mentioned in section 4.3.3, the modal damping ratios of the closed loop poles are prescribed. The cost in this is that increasing $\bar{\zeta}_j$ implies increased need of control power. The maximum prescribed modal damping ratio is chosen to be $\bar{\zeta}_j = 0.1$, where $j = 1, \dots, 2N_1$.

When the modal damping ratios of the first four unstable in-plane cable modes are prescribed according to the above, asymptotic stability of the system should be obtained. The results when these four modes are controlled are presented in the following, considering a sampling time of $300s$. The development of the control force is displayed in figure 32a and the corresponding displacement response of the cable in the damper node is illustrated in figure 32b.

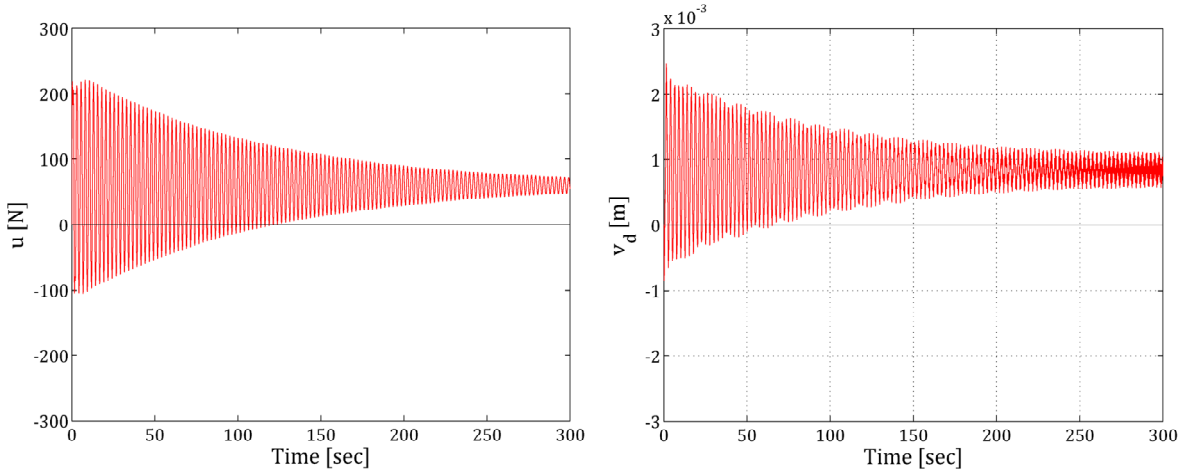

a) damper force b) cable displacement in the damper node

Figure 32: Development of the control force and cable displacement in the damper node.

According to (4.115), the control force is proportional to the part of the state vector which describes the cable motion. Hence, the static offset of the cable displacement is also represented in the control force.

A stable response of the system is obtained when the four unstable in-plane cable modes are controlled. The maximum displacement response of the cable is found at the mid-point as displayed in figure 33a. As for the linear viscous damper the displacement do not converge towards zero but a stationary peak-to-peak amplitude of $0.002m$. Compared to the reference value of the uncontrolled system, this implies a reduction of the maximum cable displacement after $100s$ by 99%.

The rivulet motion is driven by the velocity of the cable for which reason they should be damped simultaneously. In figure 33b the rivulet motion corresponding to the cable displacement as seen in figure 33a indicate that the oscillation of the rivulet is controlled when the cable is controlled.

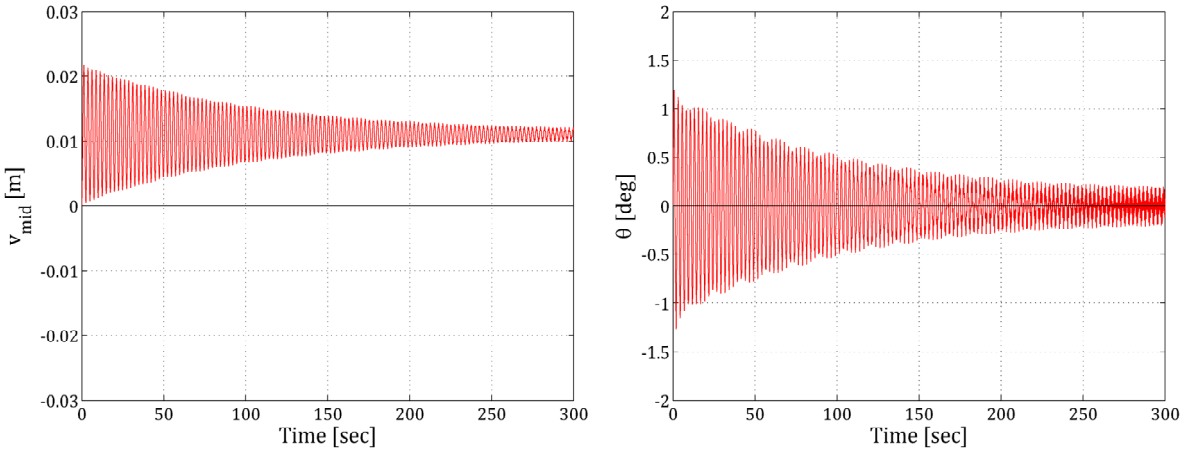

a) mid-point cable displacement

b) rivulet oscillation on an element at mid-point position

Figure 33: Maximum displacement response of the cable and the rivulet.

It is seen that active control by pole placement reduces the maximum cable displacements significantly when compared to the uncontrolled displacements and also in such a way so the system is stable if the unstable in-plane cable modes are controlled. It is found that the mean damper power reach a stationary value of $0.02W$ after $1000s$ as illustrated in figure 34.

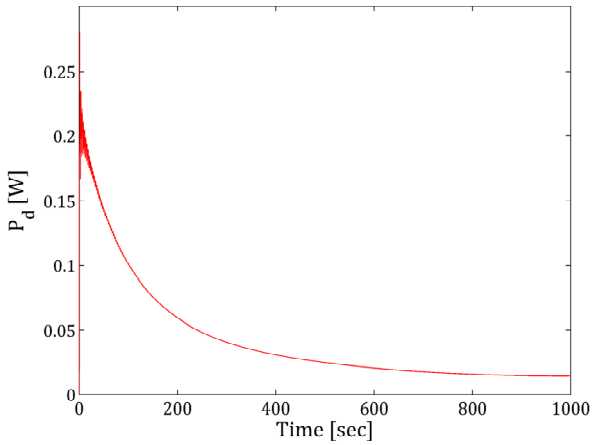

Figure 34: Mean damper power.

In relation to the way of determining the modal gains g_j as outlined in section 4.3.3 it should be noted that the remaining $2N - 2N_1$ uncontrolled modes may be subject to control spillover, which in addition to the linearized terms in the rivulet equation of motion may account for the stationary vibration level.

5.5 Active vibration control by combined pole placement and integral control

The main idea of the integral controller is to remove the static offset of the cable. At first the influence on the static displacement of the damper node is investigated. This is estimated from the time average

$$\bar{v}_d(t) = \frac{1}{t}\int_0^t v_d(\tau)d\tau \tag{5.7}$$

As $t \to \infty$, $\bar{v}_d(t)$ converge to the static offset of the damper node. In the present case, determining the optimal value of the controller gain is based on the criteria that $\bar{v}_d(t)$ converge towards zero. In figure 35a, $\bar{v}_d(t)$ is plottet as a function of the sampling time for two simulations where the response in the damper node is shown for pole placement only and when combined pole placement and integral control with an optimal choice of $\gamma_{IC} = -100N/m$ are considered, respectively. In figure 35b the corresponding damper

forces are displayed. As expected the damper force is increased when the static offset of the cable displacement is removed. Regarding the pole placement part, the first four in-plane cable modes are controlled.

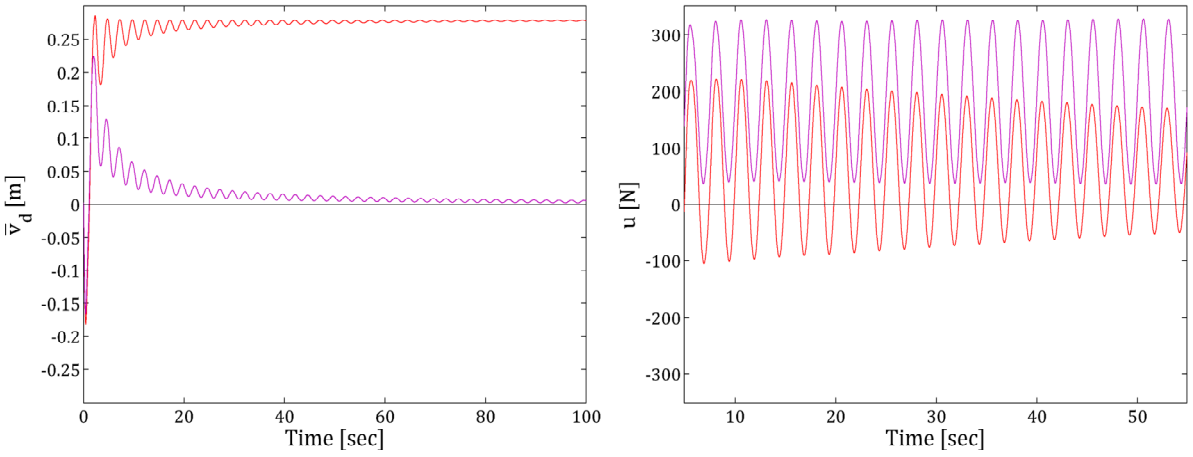

a) time averaged displacement b) damper force

Figure 35: Effects on the damper node displacement and the damper force when combined pole placement and integral control is considered.

The displacement response of the damper node is displayed in figure 36a for pole placement only and in figure 36b for combined pole placement and integral control. As seen the static offset caused by the static load component is removed when integral control is applied. However, the results also indicate that the vibration response is increased when integral control is applied. This is confirmed by calibration of γ_{IC} by repeated simulations where γ_{IC} is varied. By letting $\gamma_{IC} \rightarrow \gamma_{IC}^{opt}$, the static offset of the cable displacement is minimised. However, at the same time the vibration response of the cable is increased.

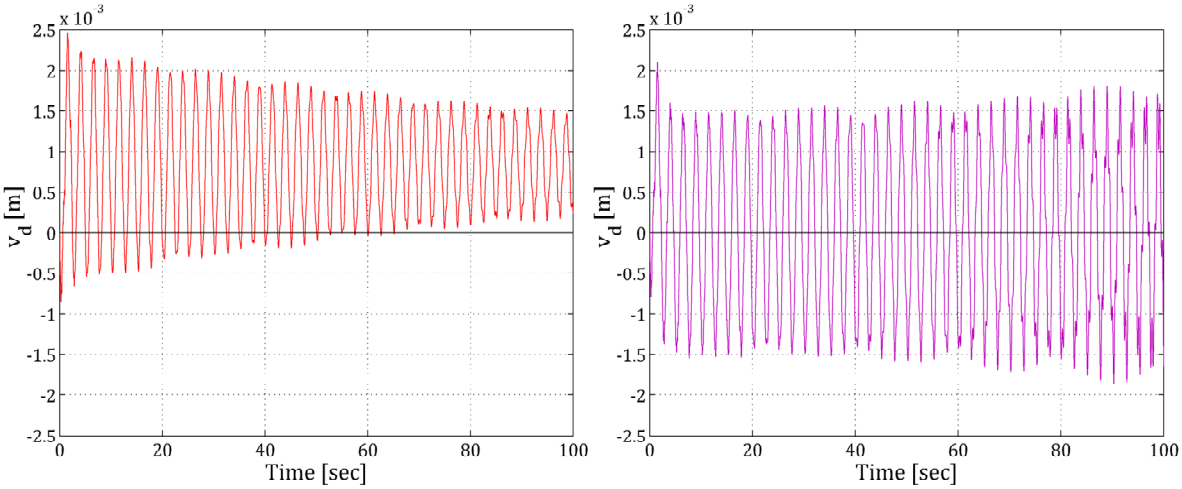

a) pole placement b) pole placement and integral control

Figure 36: Cable displacement response in the damper node

The corresponding maximum cable displacements are found at the mid-point of the cable and are illustrated in figure 37a and figure 37b, respectively. Again, the results indicate that the displacement response of the cable is increased when the integral controller is included. Furthermore, the static offset is not removed for which this is merely a local effect.

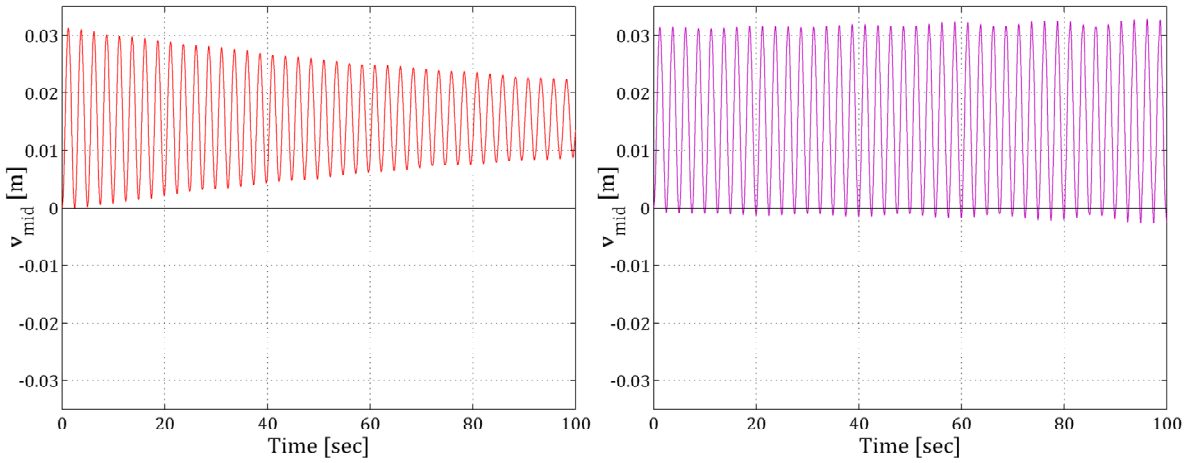

a) pole placement

b) pole placement and integral control

Figure 37: Maximum displacement response of the cable.

The results indicate that the optimal value of the controller gain is only optimal with regards to the removal of the static offset. The expected additional damping of the low-frequency modes is not observed and instead the vibration response is increased. Hence, the integral controller does not have the intended effect.

The integral control is considered separately in order to verify whether this alone or the combination with the pole placement control increase the vibration response of the cable. As seen in figure 38a the damper force have higher positive values as to account for the positive static offset. The corresponding vibration response in the damper node is illustrated in figure 38b where a comparison to the uncontrolled response is given. Again, the results indicate that when the static offset is removed the vibration response is increased.

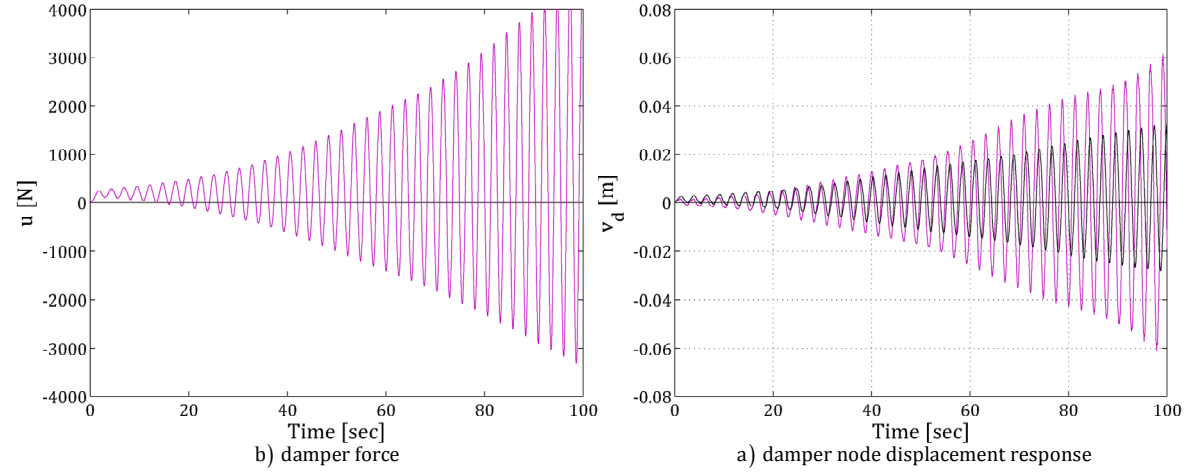

b) damper force

a) damper node displacement response

Figure 38: Results when separately considering integral control.

Furthermore, the effect is again observed to be local as the static offset is still present at the mid-point of the cable. This is illustrated in figure 39 from which it is also observed that the maximum vibration response of the cable is increased.

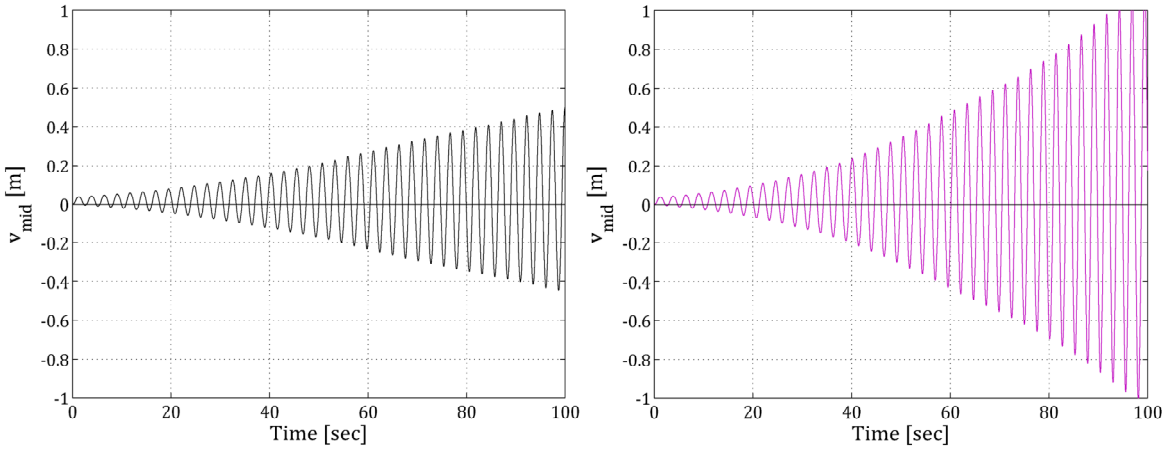

Figure 39: Effects on the maximum cable displacement when integral control is implemented.

The results from considering the integral control separately indicate that this alone is the reason for the increased vibration response.

5.6 Comparison of results

The results from the uncontrolled system, the system controlled by viscous damping, and the system actively controlled by pole placement are compared below for a sample time of $100s$. In figure 40a the vibration response of the maximum cable displacements are illustrated while the related damper forces are illustrated in figure 40b.

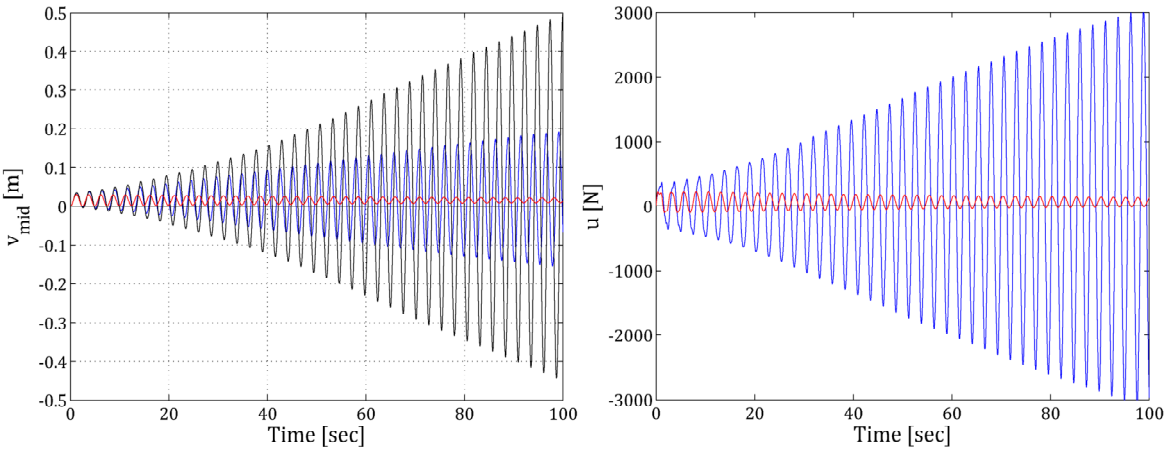

Figure 40: Comparison of results.

As expected, the active control causes a better damping of the system. It should be noted that a power source is necessary for the actuator in the active control mechanism to work.

6 Résumé

This report deals with different methods of control of rain/wind induced vibration of stay-cables.

Chapter 1:

A short introduction to the phenomenon rain/wind induced vibrations and a review of the achieved literature is given after which some different ways of controlling the vibrations are outlined

Chapter 2:

In this chapter a thorough description of the rain/wind induced vibrations is given, prior to formulating a numerical finite element model of a stay-cable inflicted by rain/wind induced loads. The analytical models formulated by *Robra* and *Yamaguchi* are shortly analysed and the expected vibration pattern are clarified. The considered cable is defined and the set-up resulting in the most severe vibration response is outlined – based on experimental results.

Chapter 3:

The basic information about the tree different types of vibration control is discussed consisting of passive, semi-active and active control. The passive control is implemented by a linear viscous damper, the semi-active control is accounted for by a MR-damping device, and the active controls are control of axial forces and control by the pole placement method.

Chapter 4:

The produced numerical model is systematically described. The quasi-static load model is derived and an equation of motion for both the rivulet and the cable is formulated. A multi-degree-of-freedom finite element model is assembled where a state vector formulation for the entire system is formulated, after which the control algorithms according to the considered damping strategies are included separately.

Chapter 5:

Finally simulations where the system is uncontrolled, controlled by passive viscous damping, controlled by semi-active damping, actively controlled by pole placement, and actively controlled by combined pole placement and integral control is conducted. The results are compared in the end in order to evaluate the relative effectiveness of the damping mechanisms.

7 Conclusion

The purpose of this thesis is to evaluate damping of rain/wind induced vibrations of stay-cables. Passive viscous damping, semi-active MR-damping, active control of axial forces, active control by pole placement, active control by integral control, and active control by pole placement and integral control are investigated in order to evaluate the relative effectiveness.

The basis is taken in a stay-cable where a rivulet is present and a uniform mean wind load is applied. Because of this, the cable vibrations consist of standing waves according to the eigenmodes of the cable. This is considered as an inadequacy of the model, since field observations show that rain/wind induced vibrations often consists of a combination of travelling- and standing waves. This is probably brought forward by randomness in the vibrations due to turbulence and randomness of the equilibrium position of the rivulets. Furthermore, the static offset of the cable displacement exist due a static load from the considered mean wind.

The theory regarding when and how rain/wind induced vibrations occur is verified and it is found that the vibrations occur only in a small interval of the mean wind velocity. Furthermore, it is proven that self-perpetuating vibrations occur when the slope of the lift coefficient $d\bar{c}_L/d\alpha$ is negative, which consist with the triggering of galloping instability, (Den Hartog, 1956). However, additional investigations should be made in order to describe the phenomenon in a more general way.

When a cable without any vibration control is considered under the worst natural loading, the first four in-plane cable modes are found to be unstable. The vibration response show that stationary peak-to-peak amplitudes are not reached, which is not in agreement with other literature. This is explained by lack of geometric non-linear stiffness terms of the cable which are ignored in the present numerical model.

When a viscous damper, tuned to the first mode of vibration of the cable is considered it is ensured that all closed loop poles have negative real part and the system is undercritically damped. Then, asymptotic stability is expected as the system is considered to be linear. However, the results show that a stationary vibration response is achieved with a maximum displacement amplitude of $0.25m$. A number of linearized approximations on terms in the rivulet equation of motion are ascribed this result. Regarding the performance of the linear viscous damper it is not possible to evaluate this result alone, since no exact field-data is available for a cable with the same dimension and setup as used in the simulation. In case of decreasing the distance between the lower support point and the connection point of the damper, relative to the length of the cable chord, the efficiency of the passive viscous damper will be reduced.

In the present case damping by the semi-active MR-damper is found to be less efficient than the passive viscous damper. If the load model is expanded to account for turbulent effects, travelling waves might be seen in the vibration response. Then, the MR-damper is expected to be more effective, since the MR-damper is capable of changing the damping coefficient in case of a sudden change in signal input. Furthermore a more comprehensive parametric study is required for the MR-damper to work more effectively. Consequently it has not been possible to achieve the same results as *Johnson*, *Baker*, *Spencer*, and *Fujino*, who claimed significant damping results, (Johnson, et al., 2007).

When the unstable cable modes are actively controlled by pole placement asymptotic stability is expected for a linear system. Instead, stationary peak-to peak amplitudes are reached in consistence with the observations from the passive viscous damping. However, when active control by pole placement is considered the maximum displacement amplitude is $0.002m$. A configuration where combined active control by pole placement and integral control is considered as the integral controller should increase damping of the low-frequency modes and furthermore remove the indicated static offset of the cable displacement. However, the results indicate that when the static offset is removed the vibration response of the cable is increased. Furthermore, the integral control will only remove the static offset locally – i.e. in the damper node.

Summarizing what is mentioned above it is found that when the active control strategy by pole placement is used, the best damping of the cable is achieved. The cost is a necessary power supply for the active control device to work, which should be evaluated in comparison to the passive device in a practical design situation.

8 Future work

In this thesis some delimitations and assumptions are made in order to complete the work within the given time period. For future work these limitations should be reconsidered in order to achieve more exact results.

First of all, the load model is based on rms-values of the aerodynamic coefficients c_L and c_D. Additional, or at least the first two, of the Fourier coefficients should be included, which in turn would require better data from tests compared to what have been available in the present case. Hereby, the memory effects on the aerodynamic coefficients could also be accounted for.

The load applied on the cable is assumed to be a constant mean wind load which is unchanged along the cable. This is a very crucial assumption, since the load in reality is varying both in height and in time due to turbulence. The turbulence u is considered as a vertical- and a horizontal component which will generate random lift- and drag forces. The vertical component is expected to affect the dynamic increment $\Delta\alpha$, while the horizontal component is expected to introduce random fluctuations of $\theta_0 = \theta_0(U_0 + u)$. This will in combination affect the effective wind angle of attack. The load may be vital in achieving travelling vibration waves of the cable. If this is done, it would be interesting to re-evaluate the effectiveness of the semi-active MR-damper.

A static offset of the cable displacement is caused by the constant mean wind load. In the active control method this is accounted for by including the integral control, but this is not the case when the passive and semi-active control is used. A combination of the viscous damper and the active integral controller could be interesting to evaluate compared to the pole placement integral control.

The numerical model which is used in the present case only takes into consideration in-plane vibrations and the applied load model is only derived for loading in the local y-direction. As rain/wind induced vibrations may consist of combined in- and out-of-plane vibrations, an extension of the model to include both types of vibrations may be preferred. If the model is extended to include out-of-plane vibrations, at least one additional damper mechanism must be included. Hence, the vibration control setup used in the passive, semi-active and active control strategy is made capable of controlling out-of-plane vibrations. If the above is implemented in the numerical model, some additional transformations are needed and the load model must be extended to account for both y- and z-directional loadings.

In general, a more detailed description of the cable motion would be obtained if the geometric non-linear stiffness terms of the cable are accounted for. Moreover it is possible to expand the equation of motion for the rivulet to include e.g. direct wind loads on the rivulet and friction between the cable and the rivulet. If these effects are included the movement of the rivulet will also depend on the size of the rivulet and the cable material. To describe these influences, additional wind tunnel tests must be performed in order to obtain a more detailed knowledge about the parameters influencing the motion of the rivulet.

The active pole placement method is a state feedback control for which reason an observer equation must be developed to express the state of the system. The observer is commonly connected to sensors mounted along the cable, but it would be preferable if a collocated observer algorithm by means of $v_d(t)$ and $\dot{v}_d(t)$ could be found.

The only restriction in the numerical model on the rivulet motion is that the simulation stops when the effective angle between the position of the rivulet and the wind angle of attack is not within a defined region. In reality the rivulet will probably disappear when inflicted by extreme vibrations, and a new rivulet will develop when the cable vibration has settled. The results from additional wind tunnel tests should be used to give a better description of the motion of the rivulet for this to be implemented in the numerical model.

9 Bibliography

BaiChay Bridge China // http://ctgttp.uct.edu.vn/photogallery/Bridge/Caudayxien/65568.JPG. - 2009.

Den Hartog J. P. Mechanical Vibrations [Book]. - New York : Dover Publications, Inc., 1956. - Vol. 4. - ISBN: 0-486-64785-4.

Fujino Y, Warnitchai P and Pacheco B. M. Active stiffness control of cable vibration [Article] // J. Appl. Mech.. - : , 1993. - 60(4). - : Vol. . - pp. 948-953.

Gu M. and Du X. Experimental investigation of rain-wind-induced vibration of cables in cable-stayed bridges and its mitigation [Article] // Journal of wind engineering and industrial aerodynamics. - 2004. - 93. - pp. 79-95.

Gu M., Du X.Q. and Li S.Y. Experimental and theoretical simulations on wind-rain-induced vibrations og 3-D rigid stay cables [Article] // Journal of Sound and Vibration. - 2008. - 320(1-2). - pp. 184-200.

Hikami Y Rain vibrations of cables of cable-stayed bridges [Article] // Journal of Japan Association of Wind Engineering. - 1986. - 27. - pp. 17-28.

Hikami Y. and Shiraishi N. Rain-wind-induced vibrations of cables in cable stayed bridges [Article] // Journal of wind engineering and industrial aerodynamics. - 1988. - 29. - pp. 409-418.

Johnson E.A [et al.] Semiactive Damping of Stay Cables [Article] // Journal of Engineering Mechanics. - 2007. - 133. - pp. 1-11.

Juang Jer-Nan and Phan Minh Q. Identification and control of mechanical systems [Book]. - Cambridge : Cambridge University Press, 2001. - Vol. I. - ISBN-13 978-0-521-03190-5.

Kovacs I. Zur frage der seilschwingungen und der seildämpfung [Article] // Die Bautechnik. - 1982. - 59(10). - pp. 325-332.

Krenk S. Vibrations of a Taut Cable With an External Damper [Article] // ASME Journal of Applied Mechanics. - 2000. - 67. - pp. 772-776.

Larsen J.W. Nonlinear Dynamics of Wind Turbine Wings [Report]. - Aalborg : Ph.D. Thesis Aalborg University, 2005.

Nielsen S.R.K Vibration Theory, Vol 1 Linear Vibration Theory [Book]. - Aalborg : Aalborg tekniske Universitetsforlag, 2004. - ISSN: 1395-8232 U2004-1.

Peil U and Steiln O Regen-Wind Induzierte Schwingungen - ein State-of-the-Ate Report [Article] // Stahlbau. - 2007. - 76(1). - pp. 34-46.

Porter B. and Crossley R. Modal control: theory and applications [Book]. - London : Taylor and Francis, 1972.

Prostas B. and Wesfreid J.E. On the relation between the global modes and the spectra of drag and lift in periodic wake flows [Article] // Comptes Rendus Mecanique. - 2003. - 331. - Vol. 1. - pp. 49-54.

Robra J. Regen-Wind-induzierte Schwingungen von Schrägkabeln und Hängern - Ein Rechenmodell zur Vorhersage und Massnahmen zur Verhinderung [Article] // Dissertation Technische Universität Wien. - 2003.

Srinivasan A. V. and McFarland D. M Smart Structures [Book]. - Cambridge : Cambridge University Press, 2001. - ISBN 0 521 65977 9.

Verwiebe C. Neue Erkenntnisse über die Erregermechanismen Regen-Wind-induzierter Schwingungen [Article] // Stahlbau. - 1996. - 65. - pp. 547-550.

Verwiebe C. Rain-wind-induced vibrations of cables and bars [Article] // Proceding of the International symposium on advances in bridge aerodynamics. - 1998. - Bridge Aerodynamics, A.A.Balkema.

Wang L.Y and Xu Y.L Active stiffness control of wind-rain-induced vibration of prototype stay cable [Article] // International Journal for Nummerical Methods in Engineering. - 2007. - 74(1). - pp. 80-100.

Wang L.Y and Xu Y.L Analytical study of wind-rain-induced vibration: 2DOF model [Article] // Wind and Structures. - 2003. - 6(4). - pp. 291-306.

Yamaguchi H Analytical study on growth mechanism of rain vibration [Article] // Journal of wind Engineering and Aerodynamics. - 1990. - 33. - pp. 73-80.

Yamaguchi H. and Nagahawatta H.D. Damping effects of cable cross ties in cable-stayed bridges [Article] // Journal of Wind Engineering and Industrial Aerodynamics. - 1995. - 54-55. - pp. 35-43.

Zhou Q., Nielsen S. R. K. and Qu W. L. Semi-active control of three-dimensional vibrations of an inclined sag cable with magnetorheological dampers [Article] // Journal of Sound and Vibration. - 2006. - 296. - pp. 1-22.